Analysis of Optothermal and Electronic Driving of Graphene Nanomechanical Resonators

by

Uriel Fernando Hernandez

A dissertation accepted and approved in partial fulfillment of the

requirements for the degree of

Doctor of Philosophy

in Physics

Dissertation Committee:

Benjamin McMorran, Chair

Benjamín Alemán, Advisor

Jayson Paulose, Core Member

Felix Deku, Institutional Representative

University of Oregon

Summer 2026

© 2026 Uriel Fernando Hernandez
This work is licensed under Creative Commons
Attribution-NonCommercial-NoDerivatives 4.0 International

DISSERTATION ABSTRACT

Uriel Fernando Hernandez

Doctor of Philosophy in Physics

Title: Analysis of Optothermal and Electronic Driving of Graphene Nanomechanical Resonators

Suspended graphene nanoelectromechanical systems (NEMS) hold promise for sensing, signal processing, and quantum technologies, but actuation methods can introduce artifacts and limit performance. We present a systematic comparison of optical and electronic driving of suspended graphene resonators across multiple devices using full and fractional factorial designs. We assess how drive and probe laser positions, actuation method, resonator size, and drive order affect access to higher-order modes and frequency stability. Using scanning interferometric microscopy and amplitude spectra, we extract modal shapes and track resonant frequency behavior over time. Optical driving provides better access to higher-order modes but causes significantly greater frequency drift than electronic driving. Amplitude and mode visibility are highly sensitive to laser positioning, and drift behavior depends on resonator size, method, and test order. Time-resolved analysis shows non-monotonic frequency drift that persists across hours to weeks, consistent with permanent changes from laser-induced damage or contaminant ablation. We also observe apparent anti-resonance behavior tied to nodal shifts at the probe position. These results clarify the trade-offs between optical and electronic actuation and establish electronic driving as the more stable option for frequency-critical applications, while providing design guidance for improving NEMS performance and reliability.

CURRICULUM VITAE

NAME OF AUTHOR: Uriel Fernando Hernandez

GRADUATE AND UNDERGRADUATE SCHOOLS ATTENDED:

University of Oregon, Eugene, OR
California State University, Long Beach, CA
University of California, Los Angeles, CA
Rio Hondo College, Whittier, CA

DEGREES AWARDED:

Doctor of Philosophy, Physics, 2026, University of Oregon
Master of Science, Physics, 2019, California State University, Long Beach
Bachelor of Science, Physics, 2014, University of California, Los Angeles
Associate of Arts, General Studies: Science & Mathematics, 2012, Rio Hondo College
Associate of Arts, General Studies: Art & Human Expression, 2012, Rio Hondo College

AREAS OF SPECIAL INTEREST:

Nanoelectromechanical Systems (NEMS)
Nanotechnology
Nanofabrication
Graphene
2D Material Transfer

PROFESSIONAL EXPERIENCE:

Graduate Research Assistant, Alemán Lab, University of Oregon, 2022-2026

Graduate Teaching Assistant, Department of Physics, University of Oregon, 2019-2026

Graduate Teaching Assistant, Graduate Internship Program Photovoltaic and Semiconductor Device Processing Track, Knight Campus for Accelerating Scientific Impact, University of Oregon, 2021-2025

GRANTS, AWARDS, AND HONORS:

Emanuel Optical, Molecular, and Quantum Sciences Scholarship, 2026

Weiser Graduate Leadership Award, Department of Physics, University of Oregon, 2024

Weiser First Year Teaching Assistant Award, Department of Physics, University of Oregon, 2020

PUBLICATIONS:

Carter, B., Horowitz, V.R., Hernandez, U.F., *et al.* A minimal-data approach for spatially resolved parameter analysis of coupled graphene nanomechanical resonators. *Sci Adv,* **11** eadq0621 (2025). https://doi.org/10.1126/sciadv.adq0621

Horowitz, V.R., Carter, B., Hernandez, U.F., *et al*. Validating an algebraic approach to characterizing resonator networks. *Sci Rep*, **14**, 1325 (2024). https://doi.org/10.1038/s41598-023-50089-1

Carter, B., Hernandez, U.F., Miller, D.J., *et al*. Coupled Nanomechanical Graphene Resonators: A Promising Platform for Scalable NEMS Networks. *Micromachines*, **14**, 2103 (2023). https://doi.org/10.3390/mi14112103

ACKNOWLEDGMENTS

Were I to properly thank everyone who made this journey possible, the total page count of this document would double. As I only have a few pages here, I will miss more than a few people, but they are no less appreciated; thank you all.

I first want to deeply thank my advisor Benjamín Alemán. His patient teaching, caring mentorship, and support throughout the program was essential and immensely appreciated. I feel especially lucky to have an advisor whom I can call my friend. I will look back fondly at our lunches, the jam sessions (even the early morning ones), the entire trip to PR (along with Ben McMorran), and the countless little moments where I felt not only heard but that my ideas and contributions were meaningful and appreciated. I will never forget, nor can I ever thank him enough, for all those phone calls that kept me going at the end.

Thank you to my committee chair, Ben McMorran, for his support and guidance, both academic and in life. As chair, even the shortest of conversations always helped push the current project forward. As a role model and mentor, I learned a lot from him about how to better navigate the world with confidence, resilience, and kindness. Thank you to Jayson Paulose for his excellent instruction and support in the classroom, in collaboration, and within the PhD committee. I am also grateful and fortunate that as a role model, he is proof that excellence in theoretical physics does not preclude care and kindness. Thank you to Felix Deku and Meredith Townsend for their support and service as committee members.

Thank you to Stephanie Majewski for her guidance and support as Graduate Advisor and for her support of me within the physics department. This dissertation is only realized because her guidance provided clear, concrete structure at a time when I physically could not muster

neither the tools nor the will to write. I am forever grateful that she believed in me even when I could not believe in myself and pushed me to the finish line.

There are countless faculty and staff to whom I am grateful but I especially want to thank H Rachelle Beach, Dietrich Belitz, Tim Cohen, Steven van Enk, Andrea Goering, Rika Ikei, Maryam Jahangiri, Laura Jeanty, Judi McDonald, Ellen Macomson, Dave Musgrove, Kayla Nguyen, Raghuveer Parthasarathy, Laurie Schneider, Brian Smith, Claire Staley, Richard Taylor, John Toner, Hailin Wang, and Nik Zhelev for their specific combinations of instruction, support, guidance, collaboration, camaraderie, and mentorship.

I am immensely grateful for the love and support of my family. Doy muchísimas gracias a mi madre y padre por su apoyo y amor. Con cảm ơn ba mẹ nhiều lắm. I also thank Martha, Carlos, Crystal, Jessica, Michael, Glory, Gilbert, Kevin (H), Gina, Kevin (N), Christina, Dustin, Alan, and all my wonderful nieces and nephews they have born.

I am fortunate to have entered this program along with an amazing cohort. Thank you all, I cherish every moment we spent together in classes, in the Binney, and elsewhere.

Thank you to all my friends back home and at Oregon. I especially thank Franscesca Ark, Matthew Brown, Sean Brudney, Gino Carrillo, Aileen Carroll-Godfrey, Kyle Cole, Haidar Esseili, Isabelle Kloc, Andrew Lesak, Ben Mannix, Maxx Miller, Sangeet Paul, Amy Soudachanh, and Valerie Vera Starling for their love, humor, and support when I needed it most.

Thank you to every member of the Alemán Lab I crossed paths with, but especially to Brittany Carter and Rachael Klaiss – for their mentorship, support, and wisdom – and Hannah Maxwell, Julien Lee, and Sophia Holland for their friendship, teaching me to be a better mentor, and allowing me to drone on far longer than is either polite or necessary.

Finally, special thank you to Dr. Dustin Destler, Samantha Oswald, the folks at UO Counseling Services, and again Benjamín Alemán, Hannah Maxwell, Amy Soudachanh, and my sisters – Martha, Crystal, and Glory.

You literally saved my life.

To Francesca and Guinness,
my two favorite beings in the entire universe.
This was only possible with your love and support.

Thank you.

TABLE OF CONTENTS

Chapter Page

1. INTRODUCTION 13

1.1 Background on NEMS Resonators 13

2. THEORETICAL BACKGROUND 17

2.1 Resonance and Resonator Coupling 17

2.2 Electronic and Optothermal Actuation of Graphene Nanomechanical Drumheads 22

2.2a Electronic Actuation 23

2.2b Optothermal Actuation 25

2.3 Design of Experiments 27

3. EXPERIMENTAL METHODS 35

3.1 Device Fabrication and Measurement 35

3.2 Factorial Experiments 40

3.3 Results 43

3.3a Fractional Factorial Results 46

3.3b Full Factorial Results 47

3.3c Methods for resonator stability experiments 49

3.3d Stability results 51

3.4 Discussion 54

4. CONCLUSION 56

References Cited 57

LIST OF FIGURES

Figure Page

Figure 2.1 Response of an oscillator under damped, driven motion..... 17

Figure 2.2 Amplitude and Phase response of a coupled resonator as a function of the frequency..... 20

Figure 2.3 A trimer..... 21

Figure 2.4 Higher order modes of a trimer 21

Figure 2.5 (Top) Weak coupling response and (Bottom) strong coupling response .. 22

Figure 2.6 Device Geometry..... 23

Figure 2.7 Example response surface 29

Figure 3.1 Square graphene resonator..... 35

Figure 3.2 Device fabrication schematic..... 35

Figure 3.3 Mounted die containing all devices used in the factorial and stability experiments..... 36

Figure 3.4 Excess graphene removal process 37

Figure 3.5 Experimental setup 39

Figure 3.6 Devices used in the full and fractional factorial experiments 40

Figure 3.7 Drive efficiency of f_1–f_4 harmonics..... 42

Figure 3.8 Scanning Interferometric Microscopy (SIM) images and Finite Element Method (FEM) simulated mode shapes 44

Figure 3.9 Data preparation 45

Figure 3.10 Frequency drift 50

Figure 3.11 Examining apparent anti-resonance..... 53

LIST OF TABLES

Table Page

2.1. Full factorial 2^2 design for a hypothetical cookie experiment 34

1. INTRODUCTION

1.1 Background on NEMS Resonators

Nanoelectromechanical systems (NEMS), devices which use electrical and mechanical processes at nanoscale, are increasingly employed and theoretically proposed as viable platforms to address needs in a wide variety of applications and research. Industrially, recent estimates for the global market for NEMS devices range anywhere from around 100 million[1] to billions[2] and hundreds of billions of dollars (USD)[3–5], where NEMS devices are harnessed for applications in data storage[6] and multi-gas analyzers[7]. On the academic side, researchers are using NEMS devices to explore polarization fields[8], as mechanical qubits for quantum computation[9], and to probe symmetry breaking dynamics at nanoscale[10]. As a result of the smaller scale, a whole host of new methods and geometries[11] have been explored to meet those new challenges. Of these new configurations, NEMS resonators[12–18] are frequently targeted for use due to their high quality factors[19] and extreme sensitivity[12,20]. To further enhance those characteristics, graphene[21–23] – an atomically thin lattice of carbon atoms – is an unparalleled fabrication material due to its low mass[24] and extremely high intrinsic tensile strength[21] (~ 130 GPa) and stiffness[21] (E ~ 1TPa). As such, graphene-based NEMS are promising platforms for a wide range of applications, including signal processing[25], advanced computation[9,26,27], and precision metrology[28]. Among these, suspended graphene NEMS resonators are particularly valuable due to their potential for exploring novel physical phenomena and enabling applications such as multi-mode nonlinear dynamics[29], resonant sensing[19,30,31], and switching[32,33].

Coupling these NEMS resonators into a network, however, presents additional challenges to explore related to the ability to scale the platforms to large networks, the ability to tune the network units and their couplings, and the persistence and reversibility of that tuning[34].

Multiple platforms have risen to address the problem of coupling two NEMS resonators together. Those that achieve tunable coupling typically do so by way of an electrostatic gate to vary that tension of the resonator[15,35] or via parametric coupling[36,37] . However, due to needing individual voltage sources for each resonator, systems that use an electrostatic gate are not scalable to high-density or large-scale networks. In the case of parametric coupling (but also in the electrostatic case), the tuning is not persistent once the voltage sources are turned off. Alternatively, passive coupling methods that do achieve scalability, such as the coupled pillar arrays proposed by Doster et al.[8,38], lack tunability as they require fabricating new devices to change the geometry of the device. To date, there is no NEMS resonator platform that achieves the industry-scale tunable resonance and coupling desperately needed to launch NEMS into ubiquity.

As a way to resolve the scalability and persistence problems of common tuning schemes, a recent tuning method has been developed by Miller et al.[34] that tunes the resonant frequency of a resonator by a completely different method than the above. In brief, the method uses a laser to create charge defects on the support substrate under a resonator membrane. These induced charges change the tension of a resonator membrane, resulting in a shift in the resonant frequency. Importantly, no individual electrostatic gates are needed for each resonator (instead just one global voltage source), the induced charges persist over a period of days, and it is fast enough to quickly tune large networks ($\sim 10^4$ resonators in 1 second). Therefore, this new method holds promise as a scalable, persistent way to tune the resonance of and coupling between resonators in large networks.

However, along the path toward realizing a scalable, fully programmable NEMS resonator network, there are multiple small, seemingly unrelated, yet persistent challenges that hound the experimental methods, discussions, and supplementary information sections of many

NEMS resonator experiments[8,10,15,39–44]. These problems include things like frequency mismatch between resonators[8], unintended frequency drift and changes[10,39,41], amplitude discrepancies[15], limited/uneven access to resonator modes and sidebands[43], etc[40,42,44]. Often these issues are mentioned as single sentences, either dismissed as insignificant, compensated for ad hoc, or accounted for by limiting the scope of the study or rolling it into an increased experimental error.

Another important aspect of these experiments is the method used in actuating the NEMS devices. Two widely used methods are optothermal laser driving[15,39] and electrostatic gate voltage driving[41,45], each offering distinct advantages. Electronic driving enables direct electrical addressability, while optical driving provides faster, contact-free actuation[46]. However, both methods introduce non-negligible effects on the system and its measured response. For instance, optical driving can shift the resonant frequency depending on laser power[19], complicating resonant sensing schemes. Additionally, the spatial position of the laser can create "dead zones" unrelated to vibrational nodes[47], potentially leading to misinterpretation of device functionality or mode presence, and thus a perceived reduction in device yield.

In contrast, electronic driving is theoretically limited in its ability to excite anti-symmetric modes due to the symmetric nature of the electrostatic force. In practice, however, imperfections such as contamination, material inhomogeneities, and fabrication defects often break this symmetry[48], making it difficult to predict or simulate device behavior a priori. Furthermore, while the efficiency of electronic driving may vary across modes, its overall actuation efficiency remains poorly understood. It is also unclear whether observed asymmetric modes are genuinely driven or arise from other effects.

Although some specific differences between optical and electronic driving are known, a comprehensive understanding of their broader impacts – such as differences in mode

excitation/suppression, access to nonlinearities, frequency and phase stability, actuation efficiency, and mode shape – remains lacking.

To address this gap, in Chapter 3 we perform a systematic, side-by-side comparison of optical and electronic actuation in suspended graphene NEMS resonators. We examine multiple devices using factorial experiments to elucidate the effects and interactions of variables such as laser position, drive method, drive order, resonator size, and time. The system response is characterized by sweeping the drive frequency to collect interferometric amplitude spectra and imaging the driven modes using scanning interferometric microscopy (SIM)[47,48]. Our results show that the positions of the drive and probe lasers significantly influence the accessibility of higher-order modes under optical driving. Generally, optical driving provides better access to these modes than electronic driving, but it also introduces greater frequency instability. Additionally, the sequence in which a device is driven affects its frequency response, highlighting the importance of drive hysteresis. These findings underscore the need for careful mode characterization in applications requiring higher-order mode access and emphasize the importance of device preparation for frequency-sensitive applications. Such considerations are essential for improving the reproducibility and reliability of graphene NEMS devices as they move toward broader adoption.

2. THEORETICAL BACKGROUND

2.1 Resonance and Resonator Coupling

Before we proceed, it will be helpful to review the salient physics of coupled resonator systems. To wit, let us begin by looking at the behavior of a harmonic oscillator that is under driven, damped motion in one dimension,

$$m\frac{d^2x}{dt^2} + \beta\frac{dx}{dt} + kx = F_0\,cos(\omega t), \tag{2.1}$$

where m is the oscillator's mass, β is the damping, k is the spring constant, and $F_0\,cos(\omega t)$ is the force driven at angular frequency ω. The response $x(t)$ of the oscillator is roughly proportional to the drive force shifted by a phase φ,

$$x \propto F_0\cos(\omega t - \varphi). \tag{2.2}$$

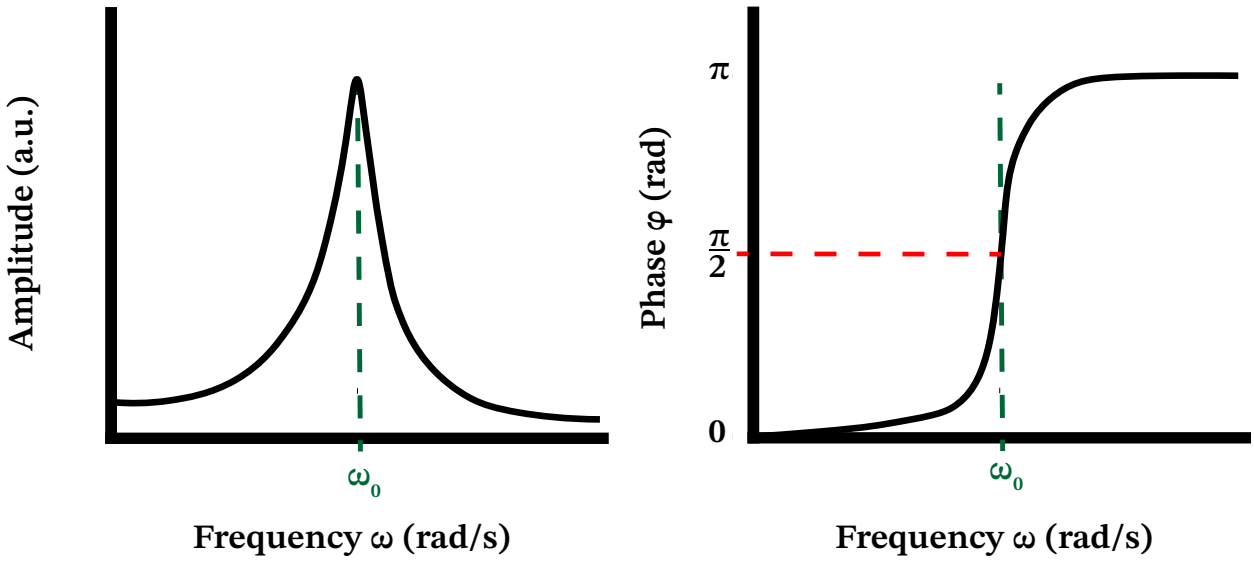


Figure 2.1 Response of an oscillator under damped, driven motion

The amplitude shows a maximum near ω_0, the natural frequency. The phase has a $\pi/2$ shift at ω_0.

We can see a better view of the response in **Figure 2.1**. By sweeping through the drive frequency, we see a maximum response of the oscillator near the *natural frequency* $\omega_0 = \sqrt{k/m}$ in the amplitude spectrum. This is an example of *resonance*, and physical systems and devices which exhibit resonance under driven motion are commonly referred to as resonators. The actual maximum – the *resonant* frequency or *resonant mode* – is at a frequency less than ω_0 due to damping. We can also see that the phase of the resonant mode always lags the drive (for non-zero ω) precisely by $\frac{\pi}{2}$ radians at ω_0 before finally maxing out at π radians as $\omega \to \infty$. We can compare this to the response of a pair of coupled oscillators. For a system with two oscillators *A* and *B*, where we drive one of the two oscillators (say *A*), we can examine the resulting mode response using the pair of equations of motion[49],

$$\begin{aligned} m_A \frac{d^2x_A}{dt^2} + \beta_A \frac{dx_A}{dt} + k_A x_A + C(x_A - x_B) &= F_0 \cos(\omega t) \\ m_B \frac{d^2x_B}{dt^2} + \beta_B \frac{dx_B}{dt} + k_B x_B + C(x_B - x_A) &= 0, \end{aligned} \tag{2.3}$$

where C is a coupling constant. In the limit where $C \to 0$, each oscillator mode reverts to that of an independent system where each of the oscillators has a natural frequency of $\omega_A = \sqrt{k_A/m_A}$ and $\omega_A = \sqrt{k_B/m_B}$ for *B*. However, when the coupling is non-zero, solving the above system of equations yields exactly two complex eigenfrequencies[49] $\omega_-(C)$ (symmetric resonance) and $\omega_+(C)$ (anti-symmetric resonance) as seen in **Figure 2.2** and given by,

$$\omega_\pm^2 = \frac{1}{2}\left[\omega_A^2 + \omega_B^2 \pm \sqrt{(\omega_A^2 - \omega_B^2)^2 + 4\Gamma^2\omega_A\omega_B}\right], \tag{2.4}$$

where now $\omega_A = \sqrt{(k_A + C)/m_A}$ and $\omega_B = \sqrt{(k_A + C)/m_B}$, to include the coupling constant, and with the frequency splitting

$$\Gamma = \frac{\sqrt{C/m_A}\sqrt{C/m_B}}{\sqrt{\omega_A \omega_B}}. \tag{2.5}$$

In order words, the single mode of the $N = 1$ system *splits* into two modes by an amount proportional to C, in the $N = 2$ case (generally, *N* resonant modes for *N* number of coupled oscillators, all moving with confined to the same, one degree of freedom). The lowest energy mode of such systems is referred to as the *fundamental mode*, while higher energy modes are *higher-order modes*.

Here we pause to present a note about the foregoing description, to clarify the analysis and terminology in following sections. As the complexity (e.g. *N* number of oscillators with *n* number of degrees of freedom) of an oscillator system increases, say from harmonic oscillators confined to movement in one-dimension, such as in these examples, to physically realized resonators moving in three-dimensions, analysis typically shifts from examining the linear mode responses (such as in this chapter) to linear and non-linear continuum descriptions. However, for many experimental resonator systems (like those used in the following experiments), where we are generally concerned with the out-of-plane motion along one dimension, modeling these systems using this linear mode treatment is still a fruitful approximation that gives us access to many salient experimental parameters. In that sense, each resonator (which in principle has an effectively infinite continuum of modes) is modeled as a harmonic oscillator whose bulk parameters such as the mass, dampening coefficient, and spring constant are approximated by *effective* mass, *effective* dampening coefficient, and *effective* spring constant in a linear modal description.

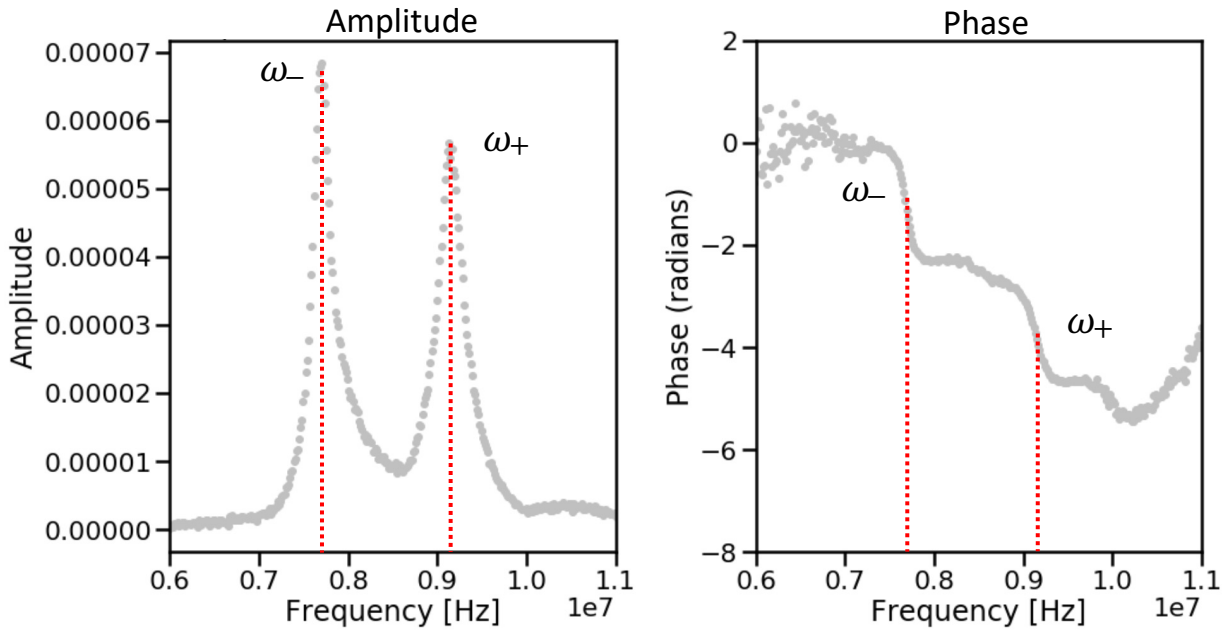


Figure 2.2 Amplitude and Phase response of a coupled resonator as a function of the frequency

The symmetric (ω_-) and anti-symmetric (ω_+) resonances are indicated by the red, dotted lines. These spectra were obtained by driving a suspended graphene resonator and measuring the amplitude and phase response of the adjacent, coupled resonator.

We can use the previous result to characterize the coupling strength of the system as the ratio Γ/γ_T, where $\Gamma = (\omega_+ - \omega_-)$ is the again the frequency splitting and $\gamma_T = (\beta_A/m_A + \beta_B/m_B)$ is the sum of the linewidths. In doing so, there are two regimes of interest[49]: weak coupling ($\Gamma/\gamma_T < 1$) and strong coupling ($\Gamma/\gamma_T > 1$). We can extend this treatment to a system with three oscillators, a trimer, where we can write Γ/γ_T explicitly as

$$\Gamma/\gamma_T = \left(\frac{k_A}{m_A} + \frac{k_B}{m_B}\right)\left(\frac{(C_A C_B)^2}{m_A m_B (k_A + C_A)(k_B + C_B)}\right)^{\frac{1}{4}}. \tag{2.6}$$

In doing so, we can model the behavior of a system where the coupling between two resonators of interest is mediated by a third, smaller resonator linking the two. An example of such a system

can be seen in **Figure 2.3**. In the limit where the size of the middle resonator decreases to zero, the system reverts to a dimer. Solving for the mechanical eigenfrequencies of the trimer system using finite element method simulations (via COMSOL[50]) for the eigenfrequencies of a linear elastic membrane, we can indeed see that we can access many similar vibrational modes that would be present in a two-resonator system with little apparent vibrational excitation of the third, intermediate resonator (**Figure 2.4a**). However, a clear difference in the dimer and trimer system is that more energy is expended in the intermediate resonator for some of the higher order modes as seen in **Figure 2.4b**.

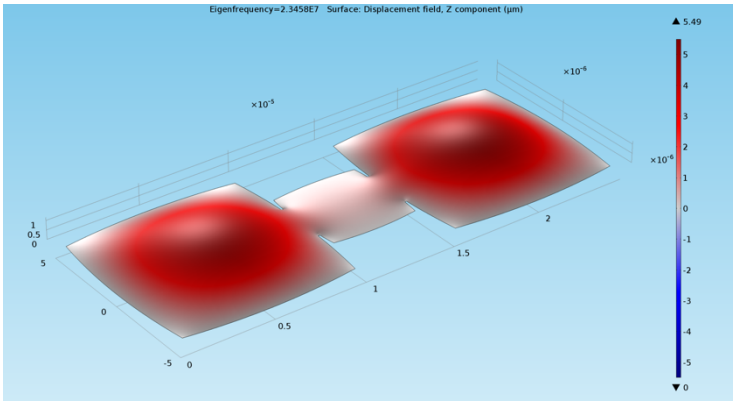


Figure 2.3 A trimer

This is a finite element method calculation using a pre-stressed, linear elastic membrane to simulate two 10μm by 10μm parabolic square resonators mediated by a 5μm-by-5μm resonator in between. This corresponds to the fundamental (i.e. lowest eigenfrequency) mode of the system.

If we sweep the drive frequency for the trimer system, as with the single resonator, and plot the behavior of the two larger resonators with masses m_A and m_B (i.e. not the intermediate resonator), we see (in **Figure 2.5**) that the spectra show the expected widening of the frequency

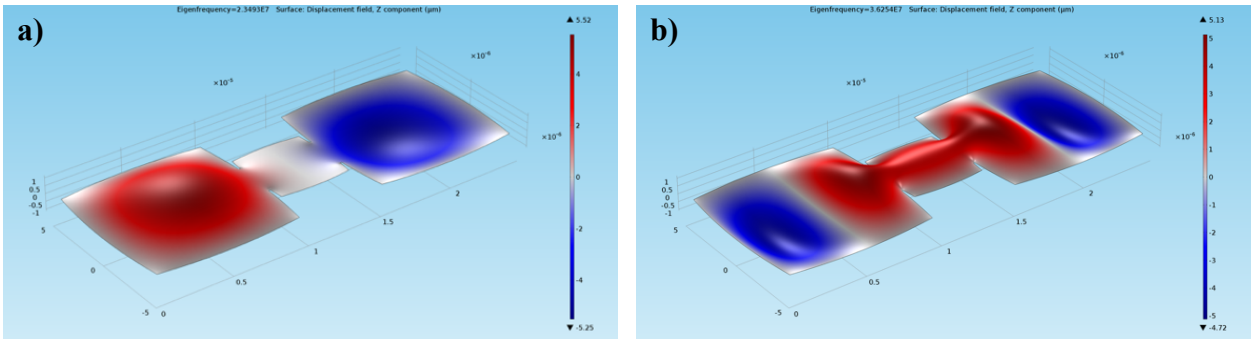


Figure 2.4 Higher order modes of a trimer

(a) A higher order mode showing expected behavior of a similar mode in a two-resonator system. **(b)** For some modes, the coupling between all three resonators is more apparent, necessitating careful modeling of a trimer, rather than a dimer, system for this kind of device geometry.

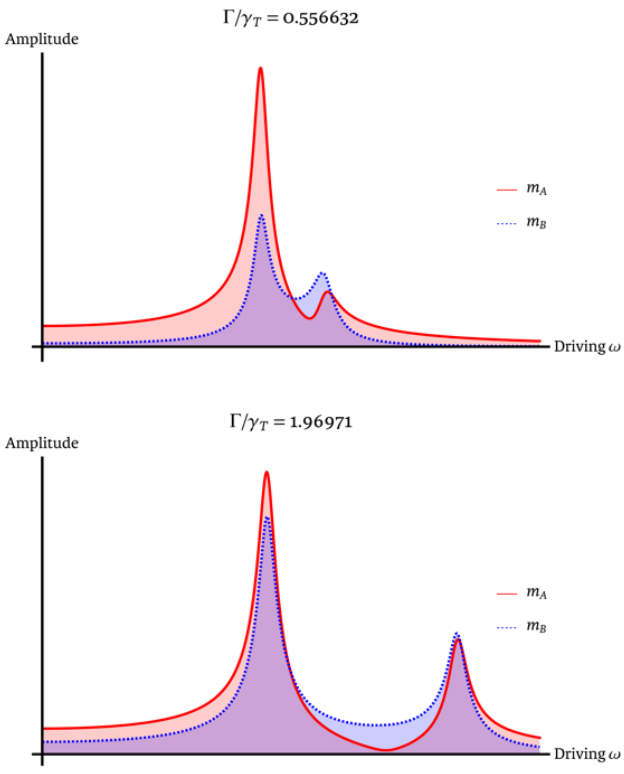


Figure 2.5 (Top) Weak coupling response and (Bottom) strong coupling response

This is the result of a numerical calculation solving for the modes in a trimer system (in one dimension) with two (nearest neighbor) coupling constants, one between mass A and the middle oscillator and between the middle oscillator and mass B. The different responses between the top and bottom plots are due simply to varying the stiffness (via the spring constant) of the middle oscillator.

splitting as the coupling strength increases. From the above, there are two results that are worth highlighting. Experimentally, we could estimate the coupling strength between any pair of resonators by measuring the drive frequency spectrum of each resonator and extracting the necessary parameters via a linear fit with initial guesses. However, if we tried to expand this to a system of N resonators, we would find the exercise intractable at larger scales. This presents a need for a faster characterization method to extract the system parameters. Second, the coupling strength, via the frequency splitting, is proportional[49] to both C and *inverse* proportional to linear combinations of k_A and k_B.

2.2 Electronic and Optothermal Actuation of Graphene Nanomechanical Drumheads

This section will provide a brief theoretical description of electronic and optothermal actuation of suspended graphene NEMS resonators. We will focus on square membrane resonators as those will be used in later sections but include an example from a circular membrane when illustrative.

2.2a Electronic Actuation

To explore electronic actuation in suspended graphene NEMS resonator devices, we can look at the device geometry that governs the interaction. For typical device geometries, graphene sheets are suspended over patterned dielectric substrates. For our purposes, we will use SiO_2 as seen in **Figure 2.6a**. Above the cavity, the device mimics a parallel plate capacitor with graphene

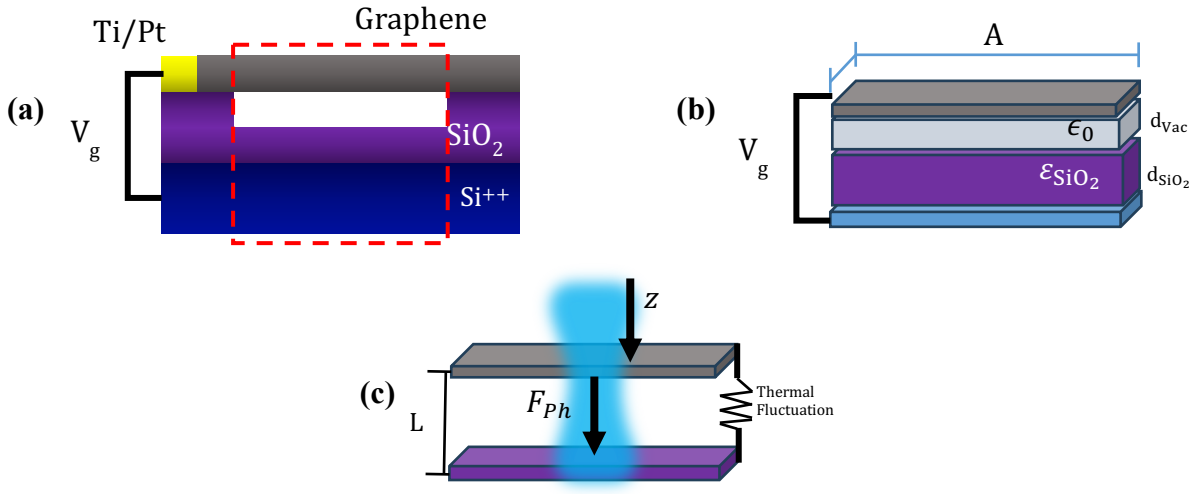


Figure 2.6 Device Geometry

(a) Graphene suspended over a patterned cavity on SiO_2, which is atop doped Silicon (Si^{++}). A gate voltage is applied on the Si^{++} and Ti/Pt contacts. The dashed line corresponds to the area of interest for both electronic and optomechanical actuation. **(b)** Effective capacitor formed by the suspended graphene and the Si^{++}. The two dielectric layers, a vacuum and the SiO_2 substrate, have corresponding dielectric constants ϵ_0 and ε_{SiO_2}, respectively. **(c)** Deformable Fabry-Pérot cavity formed by the graphene and SiO_2.

functioning as one of the capacitor plates while the doped silicon substrate acts as the other plate (**Figure 2.6b**). Interaction between the two plates is mediated by two dielectric media, a layer of SiO_2 and a vacuum. For square resonators, the device behaves like a pair of in-series parallel plate capacitors, and the total capacitance is given by

$$C_{Total} = \left(\frac{1}{C_{Vac}} + \frac{1}{C_{SiO_2}}\right)^{-1}, \tag{2.7}$$

which we can resolve using ϵ_0 as the permittivity of free space, ε_{SiO_2} as the dielectric constant of the SiO_2 substrate, d_{Vac} as the distance due to the vacuum layer, and d_{SiO_2} as the distance due to the SiO_2 substrate. The area A is the same for both sides of the plate. Accordingly, we can write the total capacitance as

$$C_{Total} = A\left(\frac{d_{Vac}}{\epsilon_0} + \frac{d_{SiO_2}}{\varepsilon_{SiO_2}}\right)^{-1}. \tag{2.8}$$

For an applied gate voltage $V_G = V_{DC} + V_{AC}$, where V_{DC} is a static DC voltage and $V_{AC} = V_0 e^{i\omega t}$ is an alternating voltage, the top plate (i.e. the graphene sheet) will experience a uniform electrostatic force, with an out-of-plane displacement x (i.e. vertically in **Figure 2.6b**), given by

$$\begin{aligned} F_{Elec} = -\frac{\partial U}{\partial x} &= -\frac{\partial}{\partial x}\left(\frac{1}{2} C_{Total} V_G^2\right) \\ &= -\frac{1}{2}\left(V_{DC}^2 + V_0^2 e^{i2\omega t} + V_{DC} V_0 e^{i\omega t}\right)\frac{\partial}{\partial x} C_{Total} \end{aligned} \tag{2.9}$$

For typical interferometric detection schemes[51], like the one used in the coming experiments, the term that contributes an alternating force at twice the drive frequency (i.e. 2ω) is not detected and hence, the force of interest on the graphene sheet is effectively[52]

$$F_{Elec} \approx -\frac{1}{2}\left(C'_{Total} V_{DC}^2 + C'_{Total} V_{DC} V_0 e^{i\omega t}\right), \tag{2.10}$$

where the first term is a uniform static force and the second term is an alternating force. In effect, the applied voltage capacitively tensions the graphene sheet via the forces in equation (2.10).

2.2b Optothermal Actuation

The mechanics of optothermal actuation in suspended graphene NEMS resonators can be modeled following the optomechanical properties of a deformable Fabry-Pérot cavity as examined by Metzger, *et. al*[53] and later Bunch, *et. al*[52]. In the model device above (**Figure 2.6a**), the graphene sheet corresponds to a mirror on one side of a low finesse Fabry-Pérot cavity (**Figure 2.6c**). For an incident laser, the force on the graphene mirror will be governed by photothermal effects (e.g. deformation of the graphene by photon heating) and radiation pressure from the conservation of momentum related to the incident photons[53]. To summarize the derivation by Metzger, *et. al*[53], the equation of motion for the center-of-mass position z of the graphene mirror, with effective mass m, mechanical damping β, and spring constant k is given by

$$m\ddot{z}(t) + m\beta\dot{z}(t) + kz(t) = F_{Th} + F_{Ph}(z(t), t), \tag{2.12}$$

where F_{Th} is a Langevin force due thermal Brownian motion, and a time-dependent, photo-induced force F_{Ph} on the graphene mirror due a weakly-modulated laser given by

$$F_{Ph}(z(t), t) = F_{Ph}(z_0) + \int_0^t \left(\frac{\partial F_{Ph}}{\partial t'} + \frac{\partial F_{Ph}}{\partial z}\frac{\partial z}{\partial t'}\right) h(t - t')dt', \tag{2.13}$$

where $h(t)$ describes the time delay due to the photon force response being retarded in time. Performing a Laplace transform and assuming exponential behavior for $h(t)$, the new equation of motion, in frequency space, becomes

$$-m\omega^2 z_\omega + i\omega m\beta_{eff} z_\omega + k_{eff} z_\omega = F_{th,\omega}, \tag{2.14}$$

where β_{eff} is a frequency space effective damping

$$\beta_{eff} = \beta\left(1 + Q_m \frac{\omega_0\tau}{1 + \omega^2\tau^2}\frac{\nabla F}{k}\right), \tag{2.15}$$

and k_{eff} is a likewise effective spring constant

$$k_{eff} = k\left(1 - \frac{1}{1+\omega^2\tau^2}\frac{\nabla F}{k}\right), \tag{2.16}$$

where $\nabla F = \partial F\big(z(t')\big)/\partial z|_{z=z(t_0)}$ approximates the partial derivative $\partial F\big(z(t')\big)/\partial z$ in the small amplitude fluctuation approximation, $\omega_0^2 = k/m$ is the resonant frequency of the graphene mirror, and $Q_m = \omega_0/\beta$ is the mechanical quality factor. Using these results and defining an effective resonant frequency $\omega_{eff}^2 = k_{eff}/m$, we arrive at the solution for the position of the mirror in frequency space z_ω, which becomes

$$z_\omega = \frac{F_{th,\omega}}{m}\frac{1}{\omega_{eff}^2 - \omega^2 + i\omega\beta_{eff}}. \tag{2.17}$$

In simpler terms, the force in the z-direction is a photothermal effect brought about by a change in the tension in the graphene sheet from laser heating, with negligible contribution from radiation pressure[51]. For example, for a circular membrane with an initial non-zero displacement of the membrane, the tension due to laser heating will obtain a non-zero component in the z-direction that depends proportionally on the incident laser power P, an initial contact angle $\theta_0 = \theta(z_0)$ between the membrane and the plane of the substrate, and inversely on the laser wavelength[51] as

$$\nabla F_{Ph} \propto \frac{AP\sin\theta_0}{\lambda}, \tag{2.18}$$

where A is a proportionality constant that depends on the material properties of the membrane (e.g. the graphene sheet). Importantly, this explains why an initial displacement (e.g. like the one achieved via the V_{DC} offset by an electronic back gate) is necessary even for purely optothermal actuation since for $\theta_0 = 0$, the change in the tension along the z-direction will also be zero (i.e. $\nabla F_{Ph} = 0$).

2.3 Design of Experiments

Before we compare the effects of the actuation methods on single graphene NEMS resonators, it is also useful to briefly overview the topic of design of experiments, including factorial analysis. In this section, we will provide a qualitative overview following the treatment and nomenclature by Montgomery in the eight edition of *Design and Analysis of Experiments*[54] and point the reader there for more details.

First and foremost, if we wish to make experimental predictions on a system, such as the effect that **changing one or more parameters** (i.e. a *treatment*) in our system has on **something we can measure** (i.e. a *response*), a few things need to present. We must be able to identify and have access to parameters (or *factors*) that we can change. We must also be able to measure any number of responses of interest that may or may not be associated with those changes. Like Montgomery, we will refer to conducting a test on any combination of purposeful changes of our input variables, to observe changes on our output responses as an *experiment*. For example, if we wanted to create a recipe for the perfect chocolate chip cookie, we might conduct a series of experimental runs to test how the amount of our ingredients (e.g. flour, salt, sugar, butter), the type of ingredients used (e.g. brown vs. white sugar or dark vs. semi-sweet, vs. milk chocolate chips), the oven temperature, and baking time affects the overall taste, texture, and color (e.g. the responses) of the baked cookies. Of course, with further thought we may be able to identify even more factors that may affect any combination of our responses or identify even more responses to measure. The factors and responses that are chosen are at the discretion of (and/or constraints on) the experimenter. Note that some of the factors can be described by a numerical quantity, such as the oven temperature, while others cannot, such as with the type of flour used. Furthermore, factors that can be described numerically can vary discretely or continuously –

either by dint of their physical constraints or at our discretion – and thus we will refer to them as *discrete* and *continuous* variables, respectively. Likewise, for factors where changes correspond not to a numerical difference but rather whether some factor within a category is included, as with the type of flour, we will refer to them as *categorical* variables.

For any given experiment, say the cookie experiment above, there are several possible ways to approach how we could test the responses of our chosen factors. In principle, given limitless time, resources, knowledge, ability, etc. we could devise an experiment that completely includes every single possible combination of treatments and measure every possible response. Despite the aspirations of some in the academy, most experimenters – unfortunately, including myself – possess neither such omniscience nor omnipotence and thus must contend with selecting which combinations of factors and responses to test in our experiments, carefully or not. Naively, we could begin our experiment with an experimental run that includes an arbitrary level for a chosen combination of factors, to establish a baseline for our responses. For a subsequent run, we could then decide to change the level of say just one factor, based on our best guess, and hold all other factors at the baseline levels. We could then proceed as such for all subsequent runs until we run out of money, materials, time, patience, or any other such real-world constraints. As of this writing, this **one-factor-at-a-time** (**OFAT**) approach is the one typically taught in undergraduate science courses and thusly employed by many, if not most, experimenters. A major flaw of the OFAT approach, besides inefficiency, is that interactions between the tested factors are generally impossible to model and often not even considered by experimenters. Thankfully, the field of **Design of Experiments** covers much more efficient methods for conducting our tests.

It might help to illustrate some of the problems with OFAT by looking at an example where it would fail. If we did possess omniscience and were able to visualize the real (but error-free, i.e. ideal) response of our system due to the effect of say two factors as a two-dimensional surface in a three-dimensional space, we could, for example, immediately choose what level for each of the two factors (e.g. bake time and oven temperature) we should choose in order to achieve a desired outcome for a response (e.g. maximize taste or achieve a certain texture) in our cookie experiment. While in the real world we do not have access to such ideal *response surfaces*, we can use the concept of them to carefully consider how we could efficiently explore the *levels* to which we set our factors to sample a desired portion of our response surface. If we think of how the OFAT approach would allow us to move through our response surface, we note that we would essentially form a line along the axis of one variable for a set level in the axis of the other one. Suppose we want to maximize the taste of our cookies, where "taste" is perhaps measured by an average numerical score assigned by a panel of expert taste-testers. Then let us assume a response surface where the taste of the cookies is plotted on the z-axis, the amount of butter is along the x-axis, and the amount of sugar is on the y-axis as in **Figure 2.7**. We will hold all other factors at some baseline level. If we follow the OFAT approach and also set the amount of sugar at the baseline level and only sequentially vary the amount of butter in out experimental runs, whether our experiment samples the global maximum for taste will depend primarily on what the real response surface looks like and in most cases on

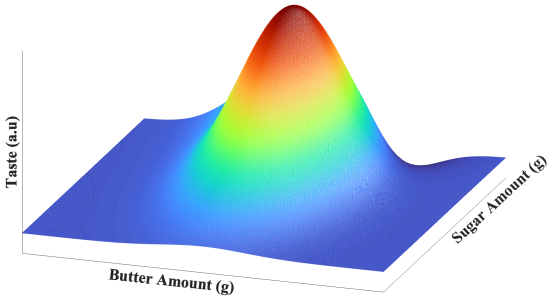


Figure 2.7 Example response surface

a whole lot of luck. For example, if the response surface is a flat plane where more butter and more sugar are each always better regardless of any other factors, then testing for the amount of butter first and then testing for the amount of sugar next might lead us to add as much butter and sugar to our cookies as possible. However, if the real response surface looks more like a mountain with one or more peaks, we might also accidentally conclude similarly depending on where and how much we sampled the response surface. This also helps us see how we would run into the problem of interactions with OFAT. For the more complicated (and more realistic) response surface in **Figure 2.7**, how much the taste of our cookies is improved by the amount of sugar might also depend on how much butter we use as well. Or the amount of butter or sugar needed to maximize our taste scores might also depend on the interaction with any number of our other factors (e.g. perhaps more butter is better up to a certain baking temperature, after which the butter burns and ruins the flavor). Thus, if we want to more effectively sample the response surface to maximize the overall taste of our cookies then we need a different approach.

Naively, if we look at the example response surface above, we could improve our chances to obtain a reasonable model for maximum overall taste by choosing a mesh of settings that uniformly samples through a sufficiently large portion of the response surface. The finer we create the mesh, by adding more experimental runs, the better our model. However, since each point in our mesh corresponds to an experimental run, real-world constraints require that we limit the number of experimental runs. Given this, we are better served by using statistics principles to determine what number of experimental runs we would need to achieve a desired accuracy for our model, and to do that we also need to take care to follow three principles when designing our experiments: **randomization**, **replication**, and **blocking**.

The most frequently used and often simplest statistical tests require that the errors in our experiment be randomly distributed and independent variables. While some dependence between the errors in the variables is sometimes unavoidable, we can maximize our success through randomization. In real-world experiments there are multiple things we can do to randomize our experiment. An important and often ignored randomization process involves resetting the experimental "knobs" available to us either when we set our factors to a given level or even of experimental settings that are fixed throughout and not intended factors. For example, in our cookie experiment, the temperature level for the baking time is often literally set by turning a physical knob. Suppose that for some reason we did not consider the oven temperature as a factor in our cookie experiment and instead chose to set the temperature knob to 375ºF for every run and that the on/off switch for our oven is separate from the knob setting. Even though the baking temperature is no longer an intended factor in our experiment, properly resetting this knob would require that for each run, we turn the knob to a setting other than 375ºF (say 0ºF) before again setting the knob back to 375ºF. In a situation where the temperature knob mechanically drifts away from the intended setting over time, say towards a higher temperature, we are inadvertently introducing the interactions between the oven temperature and the other factors into our experiment. Depending on the nature of the response surface and the range of drift in this and other un-reset knobs, the errors in our measured responses would vary with time and the order of the experimental runs becomes important. Hence, we see that failure to reset experimental knobs can result in errors that are time dependent which could cause us to incorrectly conclude correlations between certain factors that do not exist.

Coupled with resetting our knobs, we can minimize unaccounted for time dependence in our experiment by randomizing the order of our experimental runs. Often, in OFAT approaches,

experimenters run through factor levels sequentially, again introducing time dependence into their correlation analysis. Even in the case where we do not necessarily move through the surface to say maximize taste but rather want to examine the effect of two or more levels of a categorical factor, failure to randomize our experimental runs could lead to incorrect analysis of the response surface. For example, suppose we naively set our experimental runs such that, even while varying all other factors, all the runs with all-purpose flour are run first and that for all subsequent runs we switch to bread flour. If there is unaccounted for time dependence in our experiment where the taste of our cookies improves with time, we could incorrectly conclude that using bread flour instead of all-purpose flour leads to better tasting cookies.

The second important principle is that of replication, which is to say performing multiple independent runs of the same factor setting. An example of this would be if we prepare a batch of cookie dough with specific levels for our factors, bake the cookies, measure the responses, and then repeat the entire process with a new, freshly prepared batch of cookie dough and everything else at the exact same levels. Here it is important to note a distinction between a replicated run and a repeated measurement. Were we to bake the first batch, break each cookie up into multiple pieces, and have our testers measure the responses of those multiple pieces (even say, at random times in a sequence of measurements of multiple different batches), that would not count as a replicate of those factor levels, but rather a repeated measurement. Specifically, our observations would not be independent as they correspond to same, single run with a particular treatment. Contrary to a repeated measurement, a replicated run allows us to estimate the experimental error and, in the case where we try to estimate the mean of an observation, to test if there is a statistically significant difference between the levels of our factors.

The third principle, blocking, is a bit more nuanced but we can again use our cookie experiment to illustrate an example of it. Suppose that we initially started our experiment with a half-used bag of all-purpose flour and bought a fresh bag to perform the rest of our experiments. Since we are careful to buy the same brand and type, even the same size bag, we should not expect too much variation between the old bag of flour and the new one. However, it may be possible that there is a large enough difference between each bag such that it has an effect on the responses measured between batches made with either flour. There are numerous factors that can result in a difference between each flour bag (e.g. age of the flour, seasonal or intended changes in the quality of the wheat sourced, change in process by the manufacturer, etc.). Importantly, even while there may be major differences between each bag, we do not expect such nuisance factors to affect the batches made using one specific bag. Hence, we arrive at blocking, or what Montgomery calls, "a set of relatively homogenous experimental conditions". With blocking, we would, for example, pair a set of treatments in one block (i.e. one of the bags) with the same set of treatments in the other block (i.e. the other bag) for our comparisons or divide all our observations between each block and perform our statistical tests accordingly.

Following these three principles in our experimental design, we can go back to the ideal response surface and examine how we could statistically approach the number of runs we need to create a reasonable model. Suppose we only cared to test two different factors, each with two levels, say the baking temperature and baking time, to measure the effect on the texture of our cookies. To fully model the effects on each factor by itself (i.e. the *main effects*) and the *interactions* between multiple factors, we would need to employ what is (unsurprisingly) called a **full-factorial** design. Generally, a simple full-factorial design for k factors with N levels requires N^k experimental runs to achieve full replication of each factor settings. In this case,

employing a 2^2 factorial design would, at minimum, result in a list of experimental runs similar to that in **Table 2.1**.

While the 2^k design is typically tractable and effective for screening a system for the effect of a small number of factors with two levels, since the complexity of our experimental design grows exponentially for the N^k full-factorial, constraints will usually result in a compromise between the number of factors or levels in a single experiment or limiting accessibility to higher-order (or all) interactions in our model. For most screening experiments, where we might only want a quick initial survey of salient factors and maybe interactions between sets of two factors (i.e. 1st – order), a **fractional factorial** design allows us to retain all factors and levels, at the cost of higher-order interactions, while reducing the number of runs needed for our experiment. In fractional designs, the N^k full-factorial is carefully modified as N^{k-p}, where p is an integer that describes the reduction in the number of runs by halves (e.g. $p = 1$ is a $1/2$ reduction, $p = 2$ is a $1/4$ reduction).

	Pattern	Baking Temperature (ºF)	Bake Time (minutes)	Texture Score
1	− −	325	12	•
2	+ +	400	18	•
3	− +	325	18	•
4	+ −	400	12	•

Table 2.1 Full factorial 2^2 design for a hypothetical cookie experiment

The – and + in the Pattern column correspond to the low and high levels of the Baking Temperature and Bake Time factors.

3. EXPERIMENTAL METHODS

3.1 Device Fabrication and Measurement

To compare optical and electronic actuation in suspended graphene NEMS resonators, we fabricated square graphene drumhead devices (**Figure 3.1**). These devices were fabricated using standard photolithography to etch square SiO_2 cavities and deposit a 10/40 nm layer of Ti/Pt electrodes on a commercially[55] grown wet oxide SiO_2/Si substrate as outlined in **Figure 3.2**. Bi-layer graphene was suspended over the prepared

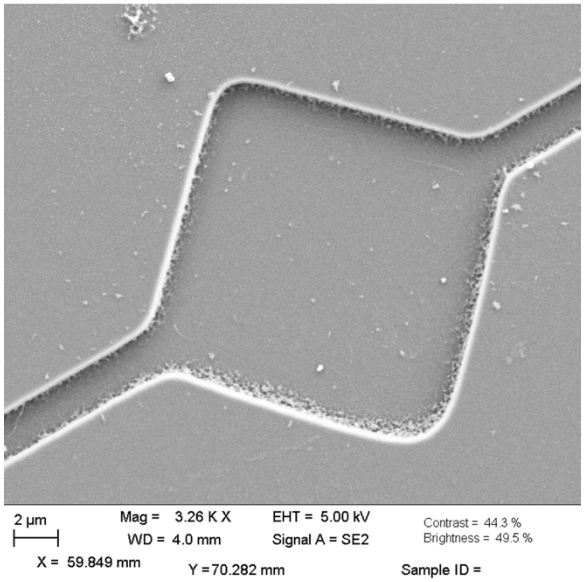


Figure 3.1 Square graphene resonator

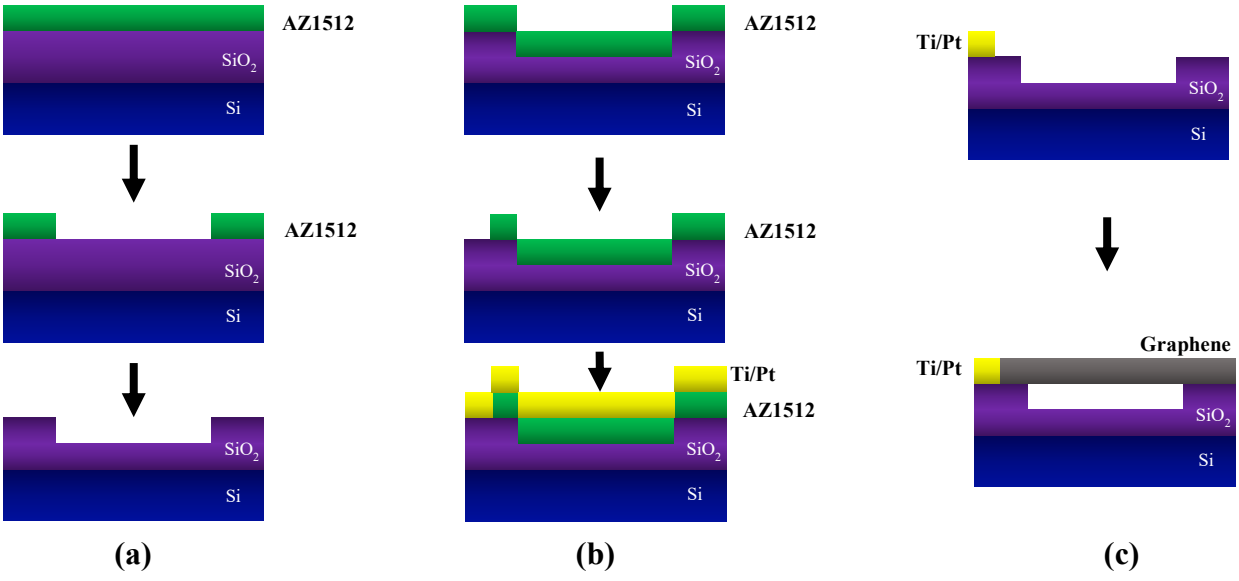


Figure 3.2 Device fabrication schematic

(a) A Si/SiO_2 substrate coated with AZ1512 photoresist, the patterned resist to protect against etching, and the etched substrate. **(b)** More resist is applied, patterned, and 10nm of Ti and 40nm of Pt deposited on substrate. **(c)** Excess metal lift-off leaves Ti/Pt electrodes on a substrate with patterned cavities and the graphene transferred onto the patterned substrate.

substrates by Graphenea[56]. Further fabrication details for this part of the process can be found in Brittany Carter's PhD dissertation[57].

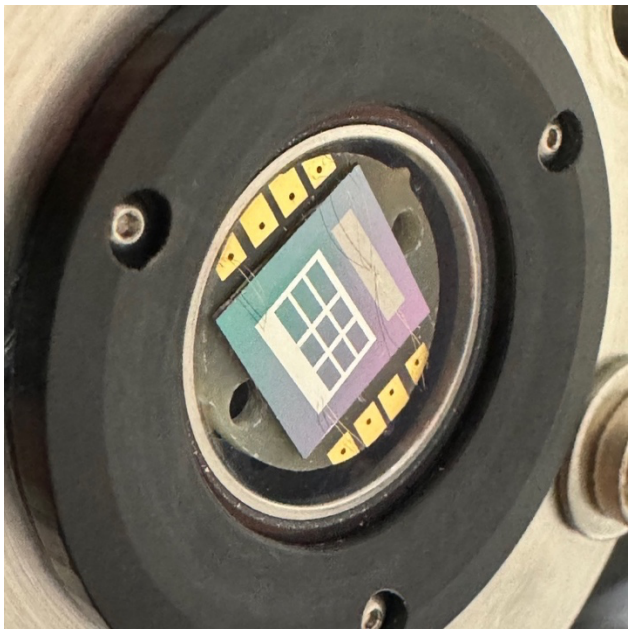


Figure 3.3 Mounted die containing all devices used in the factorial and stability experiments

Once the graphene was transferred onto the prepared substrate, the entire die is in a short-circuited state since the graphene covers the entire surface and there are multiple electronic contacts (see **Figure 3.3** for die geometry). Accordingly, we devised a simple method to cleanly remove the excess graphene from unintended surface areas based on a similar dry-transfer technique[58]. As a brief overview, the goal is to cover the area on the die where we want to keep graphene with a mask that will resist the heavy oxygen plasma etching required to remove graphene. Contrast to other methods that pattern graphene using photoresist as a soft mask[59], we wanted a process that neither leaves a residue on the graphene membranes nor risks damaging them. The latter is especially important as typical patterning processes deal with graphene directly in contact with the substrate rather than suspended membranes. Moreover, as the dies needed to be shipped overseas to complete the 2D graphene transfer (a process with takes ~2 months) and previous failed attempts to establish an open circuit on other dies left us with only one viable die, the new removal process needed to be undoable with minimal damage to the membranes in case of failure.

The process begins by gently taping a small strip of double-sided polyimide tape (e.g. Kapton® tape[60]) onto a clean glass slide that contains previously added measurement markings of a desired shape on the opposite side. As the polyimide tape is translucent, the markings provide

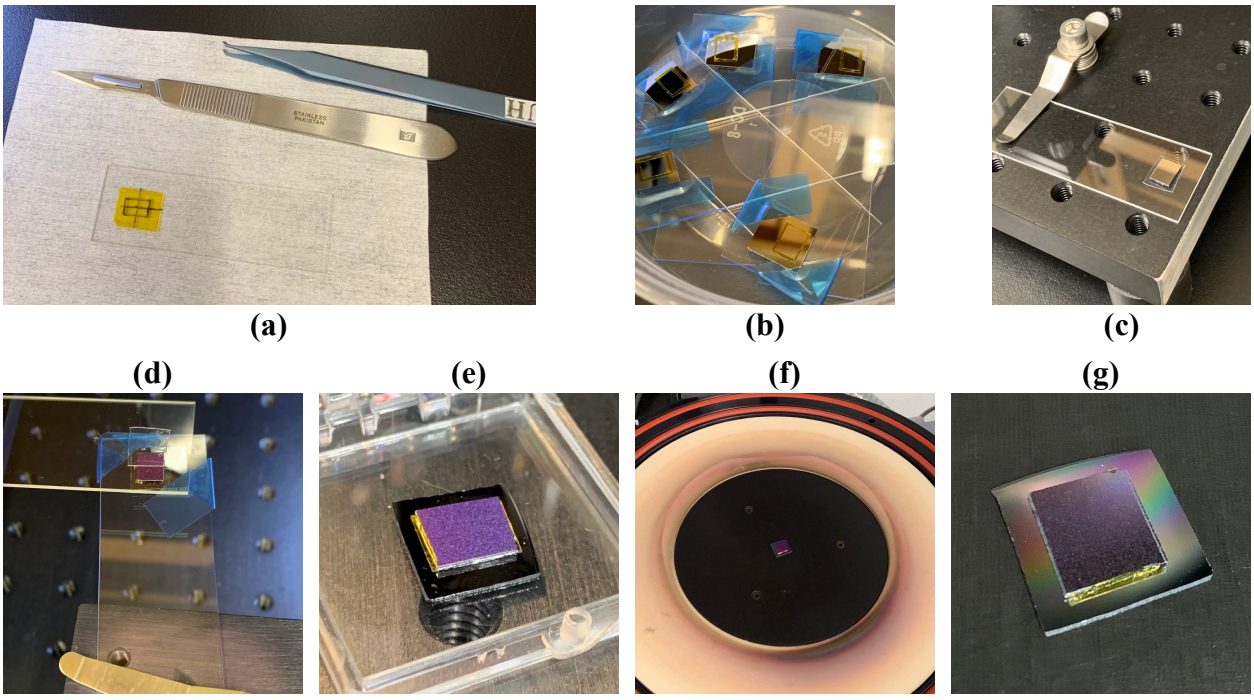


Figure 3.4 Excess graphene removal process

The images here are from the process development before it was implemented on a real device. **(a)** Polyimide tape on glass slide. **(b)** Trimmed rectangular polyimide rings on silicon dies. **(c)** Si cover mounted on polydimethylsiloxane (PDMS). **(d)** Top glass slide brought back up after depositing the cover in (c) onto a die in (b). **(e)** A prepared die before undergoing plasma cleaning. **(f)** Die in (e) inside a plasma etcher. **(g)** Cleaned die.

guidelines for both the inner and outer diameter of a rectangular ring (**Figure 3.4a**). We kept the PET liner on the top side of the tape to keep the shape rigid for the cutting step. Using a long working distance objective and a #11 surgical scalpel, we carefully trimmed the rectangular rings and lift off the unwanted polyimide tape using tweezers. We then mount the graphene-coated die onto a clean glass slide and tape the edges with low-adhesion tape (**Figure 3.4b**). In contrast to the sheet of polydimethylsiloxane (PDMS) used in the Yang *et. al*[58] and later steps to mount e.g. substrates, the tape is important in this step as the relatively high adhesion of the polyimide tape would lift the die off the glass slide. After removing the PET liner from the polyimide ring, we aligned and lowered the glass slide with the ring onto the glass slide with the taped die. After we

ensured that the polyimide ring is in full contact with the die, we slowly lifted off the top glass slide while carefully using a razor blade to separate the ring from the glass slide, as needed. This resulted in a protective ring, approximately 60μm in thickness, with high thermal and electrical insulation needed to protect the graphene membranes in later processing steps (**Figure 3.4b**). We then mounted a small silicon die cover, approximately the same area as the polyimide ring, onto a sheet of (PDMS) on a clean glass slide (**Figure 3.4c**). Like before, we lowered the mounted Si cover onto the device die and lifted off the top glass slide (**Figure 3.4d**), resulting in a protected sample (**Figure 3.4e**) that was ready for plasma cleaning (**Figure 3.4f**). We then cleaned the sample using a March CS-1701 Reductive Ion Etch (RIE) system for 300 s under 250 mTorr of pressure, 100 W of power, and no O_2 gas (i.e. used only inert Ar gas to ablate residue/graphene from the surface), which resulted in a clean surface as in **Figure 3.4g**. Finally, we taped the cleaned die a clean glass slide and removed the polyimide ring and Si cover using the long working objective, tweezers, and a razor blade. Once we tested the electrical contacts to ensure we fixed the short circuit, we mounted the die to a custom ordered PCB and bonded gold wire to multiple contacts using a West Bond Model 747677E wire bonder (see **Figure 3.3**).

With the devices ready, we used two driving methods, optothermal and electronic driving (**Figure 3.5b,d**). Under optical driving, the intensity of a 435 nm diode laser is modulated using an acoustic optical modulator (AOM). For electronic driving, a DC bias V_{DC} is coupled to the RF signal V_{Drive} from a lock-in amplifier (LIA; Zurich Instruments HF2LI) using a bias tee, which is then applied across the top Ti/Pt and the bottom doped-Si gate electrodes. For both schemes, a 633 nm probe laser measures the displacement amplitude interferometrically as it reflects off the surfaces of the membrane and SiO_2, and its signal is measured via an avalanche photodetector (APD) and lock-in detection. The position of the probe laser is adjusted using a fast-scanning

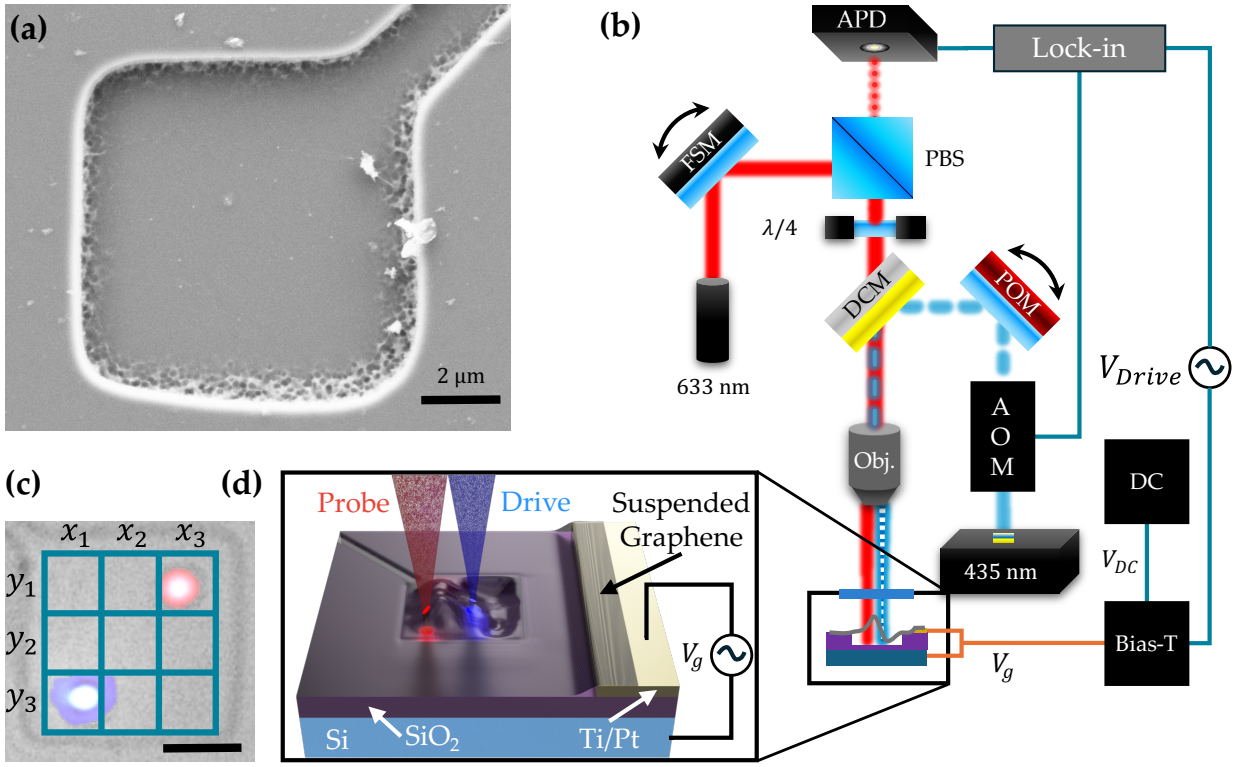


Figure 3.5 Experimental setup

(a) Scanning Electron Microscopy (SEM) image of a typical suspended graphene device under test. **(b)** Schematic of the experiment setup showing both optical and electronic driving schemes. **(c)** An image of a resonator with a superimposed diagram of the approximate laser position grid. The scale bar is 5 µm. **(d)** Diagram of a device and the different drive methods employed.

mirror (FSM), while the drive laser position is adjusted using a mirror on a piezo optical mount (POM). The electronic bias, electronic drive amplitude, 435 nm laser amplitude, and the two laser powers (before modulation) were kept constant throughout experiments. We controlled the power of the 435 nm drive laser via a PID loop and used an intensity-stabilized 633 nm HeNe laser (Thorlabs HRS015B) as the probe laser. The probe laser was allowed to stabilize for one hour before measurements. These two schemes allow us to easily switch between optical and electronic driving and change the positions of both laser spots (**Figure 3.5c**), while recording the frequency spectra and SIM mode shapes[47,48].

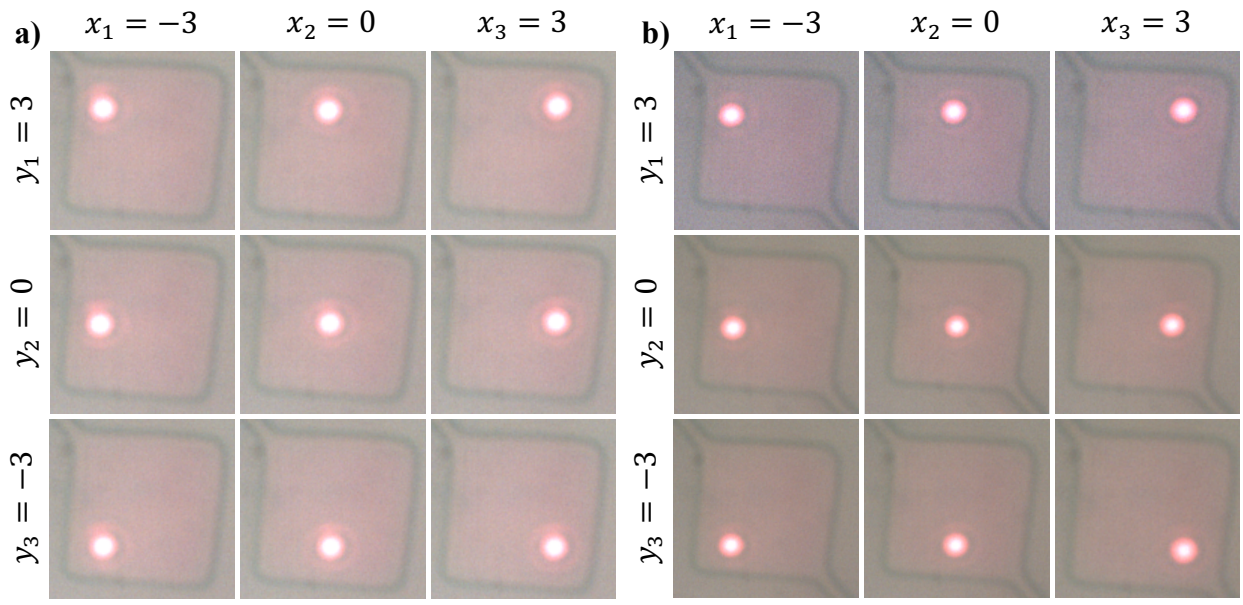


Figure 3.6 Devices used in the full and fractional factorial experiments

(a) All nine laser positions used on Device 1. **(b)** All nine laser positions used on Device 2. Each of these two devices are square suspended graphene resonators and 12 μm in width.

3.2 Factorial Experiments

Without *a priori* knowledge of the mode shapes on a given resonator, we could in principle map out the effect that the probe laser position has on the output measurement by changing the position of the probe laser such that is completely spans a given resonator surface. If we use a 12μm x 12μm-sized square resonator such as the ones in **Figure 3.6**, and with a probe laser linewidth of ~1μm[47] for our system, we would need to change the probe position 144 times, while taking an ~30 minute spectrum of the frequency such as in **Figure 3.7a** at each position. At approximately 72 hours of work, that is not very onerous. If we also wish to incorporate the effect of the laser drive position *at a single probe laser position*, that is also only another 72 hours of work. However, proceeding in this fashion to include the interaction between the probe and drive laser positions, for all 20,736 possible combinations, would amount to over 10,000 hours of work just for one device. Moreover, incorporating any number of other effects

such as the effect of electronic driving or different device sizes would quickly render the endeavor intractable during the span of a single PhD. As such, here we employ the use of factorial design as discussed in **Section 2.3** above.

To test the effect of both laser positions, we employed one full factorial and four fractional factorial designs using a 3 × 3 grid of spatial locations on two square-shaped graphene membrane resonators, both 12 μm in width (see **Figure 3.5c** and **Figure 3.6**) The fractional designs sample 18 combinations of X and Y probe positions for each drive method, for each device and in random order. The full factorial sampled all 81 combinations of X and Y positions on one device with optical driving, in random order. The factors included the X and Y positions of the drive and probe lasers (3-levels each) and the drive methods (2-levels). The frequencies and amplitudes of the first five resonant frequencies (i.e. $f_0 - f_4$ modes) comprised the response variables (**Figure 3.7a**). We prepared the response spectra using MATLAB [61] to programmatically extract the mode frequencies and amplitudes. We created and analyzed all designs using JMP software [62].

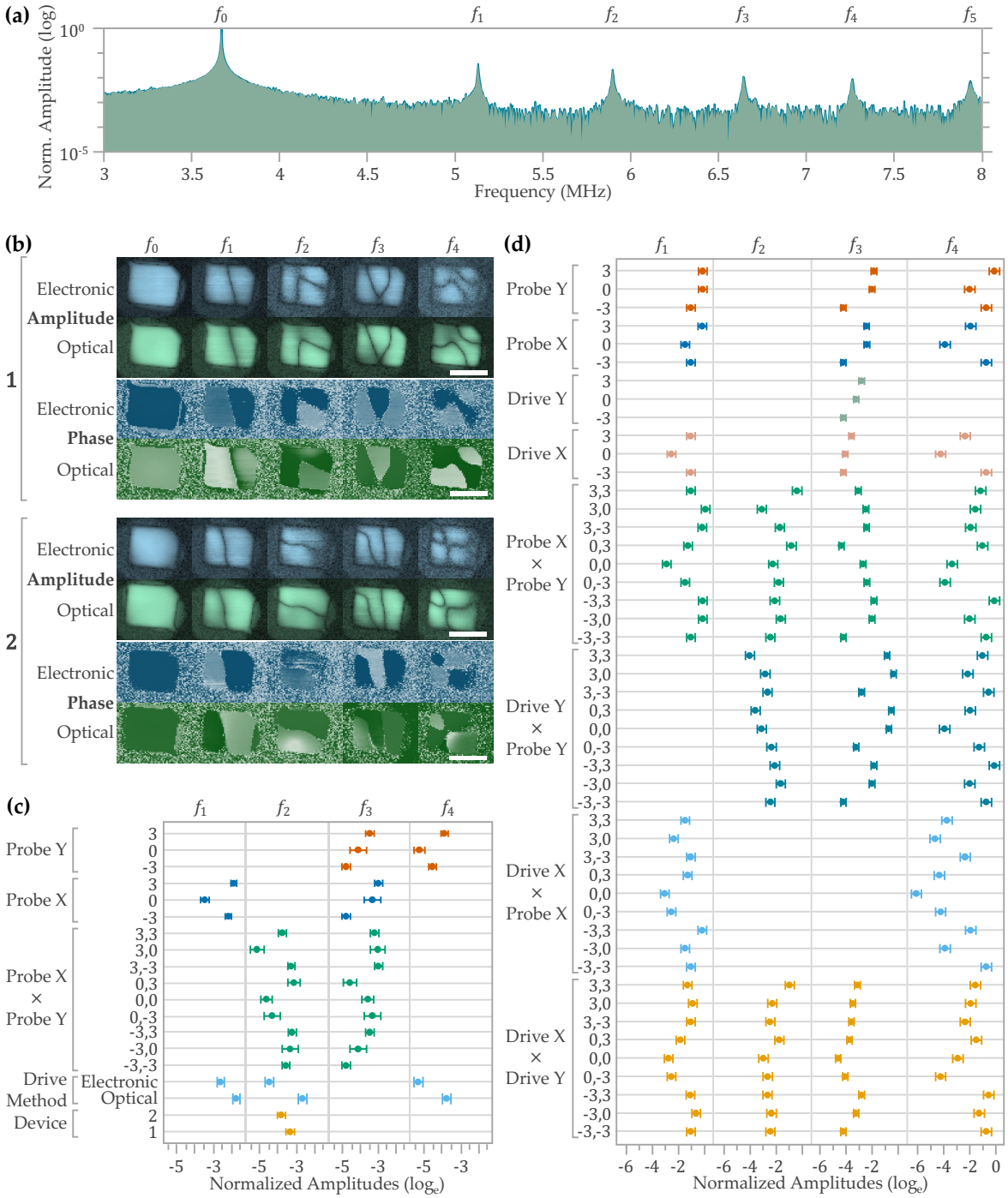


Figure 3.7 Drive efficiency of f_1–f_4 harmonics

(a) Frequency spectrum normalized to the fundamental mode f_0 and scaled logarithmically. **(b)** Amplitude and phase mode shapes for f_1–f_4 obtained using scanning interferometric microscopy (SIM) for devices 1&2. Scale bar is 10μm. **(c)** Mean ln-normalized amplitudes of f_1–f_4 for main effects and interactions with $p < 0.05$ from a fractional factorial experiment on devices 1&2 in (b). **(d)** Mean ln-normalized amplitudes of f_1–f_4 for main effects and interactions with $p < 0.05$ from a full factorial optical experiment on device 1 in (b).

3.3 Results

To determine whether optical and electronic driving methods excite equivalent modes, we used SIM to spatially map the amplitude and phase response of each resonator across the first five modes $(f_0 - f_4)$ for both actuation methods (**Figure 3.8**). The resulting SIM images show qualitatively similar nodal and antinodal structures in both size and shape across the two methods. However, amplitude images from electronic driving exhibit slightly lower contrast and increased granularity, consistent with a reduced signal-to-noise ratio. Despite these differences, the overall mode shapes are qualitatively similar between optical and electronic actuation for a given device. The mode shapes also differ from device to device, indicating that simple models of these shapes will likely fail. An example of this can be seen when comparing the finite element method simulations for the mode shapes to those obtained via experiment for both devices (**Figure 3.8**). Also, the node structure shows that the positioning of the probe laser is crucial to observe certain modes, since locating the probe on a node will result in no or poor signal and noisy phase.

Prior to modeling the main effects and interactions of our factorial designs, we mitigated differences in the variance of our responses (i.e. heteroscedasticity) due to uncontrolled factors such as differences between each device (e.g. geometry, strain, etc.), in the forcing from each

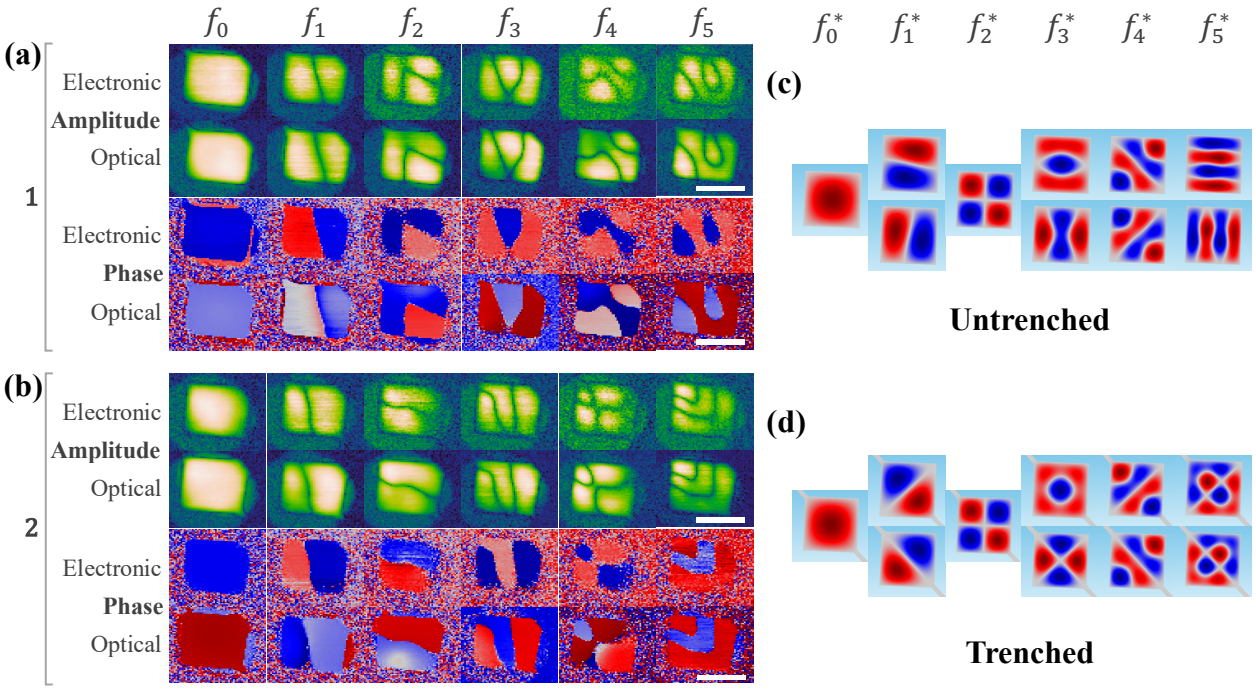


Figure 3.8 Scanning Interferometric Microscopy (SIM) images and Finite Element Method (FEM) simulated mode shapes

SIM images of the first six measured frequency resonances (labeled $f_0 - f_5$) for the amplitudes and phases of **(a)** device 1 and **(b)** device 2 for both optical and electronic actuation methods. The FEM simulated mode shapes (labeled $f_0^* - f_5^*$) are the eigenfrequency solutions to a pretensioned, square vibrating membrane with **(c)** untrenched and **(d)** trenched geometries. The simulated mode shapes contain degeneracies for f_1 and $f_3 - f_5$. The scale bars are 10μm.

method, and in the overall amplitude/noise floor of each run. Thus, we normalize the raw amplitudes A_i (**Figure 3.9a**) at each mode to the amplitude A_0 at the fundamental frequency f_0 of each spectrum. Moreover, to further minimize heteroscedasticity, we transformed the normalized amplitudes by their natural logarithm (**Figure 3.9b**). Hence, we examined the

$\log\left(\frac{A_i}{A_0}\right)$ distributions of each mode for both the fractional (**Figure 3.7c**) and full factorials (**Figure 3.7d**) using least squares regression, separately.

For the four fractional factorial experiments on both devices, we performed a least-squares modeling of the effects/interactions of the probe X and Y positions and the drive method. We incorporated a nominal variable for the device (i.e. 1 or 2) as a blocking variable. For each mode, we reduced the model until only effects and interactions with p-values $P < 0.05$

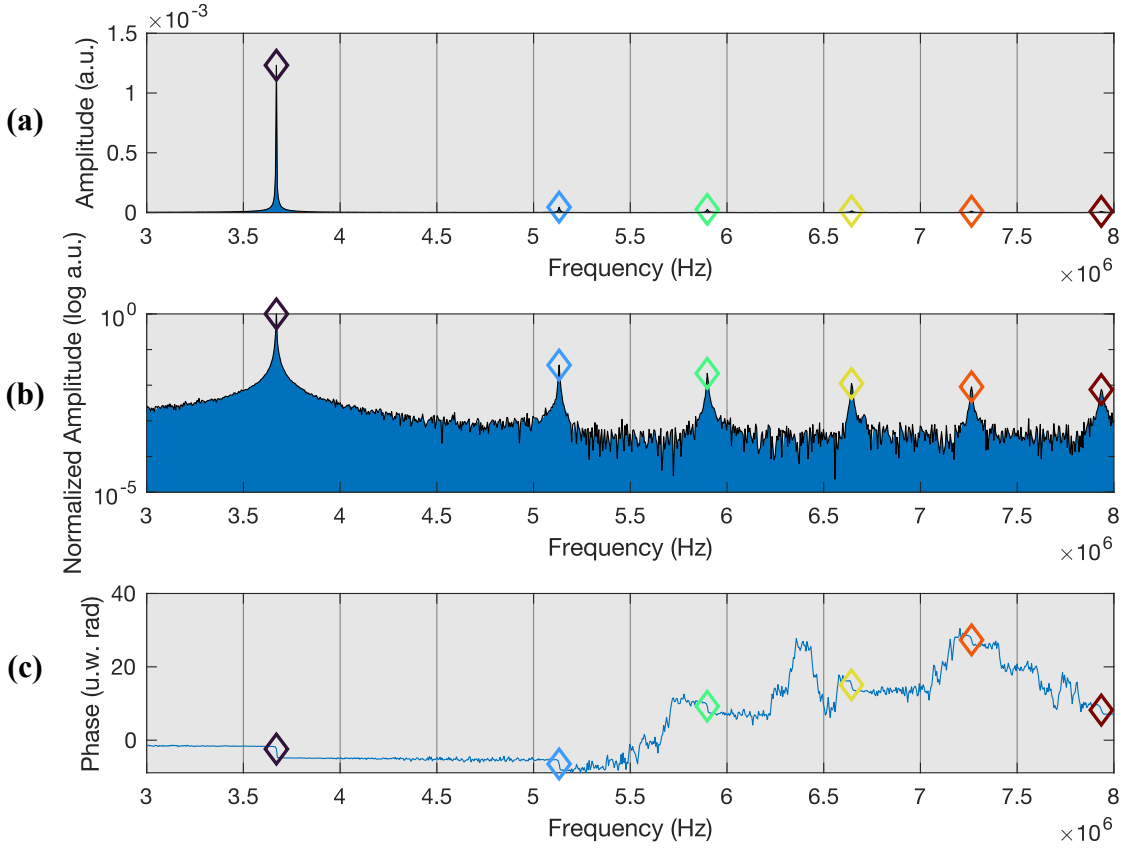


Figure 3.9 Data preparation

(a) Raw amplitude data with diamond markers at the locations of resonance modes. **(b)** The data are normalized to the amplitude of the first resonance peak and then modified by their natural log. **(c)** Phase data with diamond markers corresponding to resonance peaks in (a) and (b).

remained, while preserving model hierarchy. The least-square means plots for this reduced model is shown in **Figure 3.7c** for the fractional factorial and **Figure 3.7d** for the full factorial.

3.3a Fractional Factorial Results

The fractional factorial lets us explore differences in the two devices, the coupling of probe position by itself, and the interaction with the drive method. The benefit of the fractional factorial design is that it lets us include the drive method and device factors without paying a heavy penalty in experimental runs.

For f_1, the probe's X position, and the drive method had a significant effect. There is enough similarity in devices to remove it as a block variable in the model. There is only X-dependence, indicating asymmetry in this axis, in agreement with the SIM scans where we see a large dip in amplitude near $X = 0$. The Y probe position is consistent across the probed X positions, also consistent with SIM maps. The optical drive had larger signal than the electronic.

For f_2, the probe's X and Y position interaction, the drive method, and the device, had a significant effect. The device factor indicates a difference between this mode, consistent with SIM maps; f_2 mode for device 1 has an "L" shaped lobe in the upper-left of the device, and a square lobe in the lower right. The L lobe also has a minor node across it. The f_2 mode shape of device 2 is the expected horizontal degenerate mode of f_1. The $X \times Y$ interaction term means that the X position affects the Y position's effect on the amplitude and is seen simply as statistically varied amplitude with position. The $X \times Y$ interaction is dominated by the minimum amplitude at $X, Y = 3{,}0$ – where both devices have a horizontal node – and lower amplitudes at $X, Y = 0{,}0$ – the inner corner of the L – and $X, Y = 0, -3$, which is likely affected by the node of device 1. Lastly, the optical again has larger amplitude.

For f_3, the probe's X position, Y position, and $X \times Y$ interaction had a significant effect. For f_4, the probe's Y position, and the drive method had a significant effect. The device and drive method do not predict the amplitude, suggesting that the mode shapes are similar enough where probed, consistent with the SIM images. The results are averaged over all nine drive positions. The highest amplitude is when $X = 3$, and $Y = 3$.

For f_4, only the probe's Y position and the drive method predict the amplitude. The device block factor vanishes, so this mode will look different for each device, consistent with SIM scans. Optical driving again has a larger overall amplitude. The absence of X-dependence may be due the complex structure of the mode, yet the probed points at all Y positions persist. The amplitude has a drop at $Y = 0$, where both devices have near horizontal node across, and maxima at $Y = -3{,}3$ where the probe samples mode lobes.

3.3b Full Factorial Results

Here we explore the interactions between the drive and probe laser positions under optical driving. The main question we wish to address under optical driving is how the drive and probe lasers interact. Our previous work showed some interesting effects[47]*, but the parameter space is huge, so factorial design allows us to explore this in an efficient way.*

We performed a similar least-squares regression on the full factorial experiment. As we did not have different devices or methods to confound our results, and we sampled all 81 combinations of X and Y positions from both lasers, we were able to model the interactions between the probe and drive lasers. As before, we fit and reduce each mode separately, preserving hierarchy.

In **Figure 3.7d** we similarly only display effects and interactions for which $p < 0.05$, for clarity. Here, we see that the probe X position and probe Y position had a significant effect on modes f_1, f_3, and f_4. However, the interaction between the probe X and Y positions had a significant effect on all modes. The interaction follows the lobe and node structure of the modes seen in **Figure 3.7b**, with low signal over nodes and high signal over lobes (antinodes). In accord with the fractional results (**Figure 3.7c**), the signal measured at a fixed position varies from mode to mode. For example, the signal at position $X, Y = 0,3$ is the lowest measured for f_3, but has one of the highest amplitudes for f_4.

The drive X position had a significant effect on modes f_1, f_3, and f_4 , while the Y position only had a significant effect on f_3; the Y position leads to decreased amplitude as Y varies from 3 to -3, while the $X = 0$ position had the smallest amplitude. As with the probe X and Y positions, the X and Y interaction of the drive laser had a significant effect on all modes as well.

There was a significant interaction between Probe Y and Drive Y for modes f_2, f_3, and f_4. If we examine the difference between the smallest and largest mean, the biggest difference for f_2 is 2.33 ± 0.50 (ln-scale) or a difference of ~10.4x. For f_4 the biggest difference is 3.78 ± 0.51 (ln-scale) or a difference of ~44x. We can say that this large difference does add extra caution to the relative positioning of the drive and probe lasers. Some modes matter and some do not. Here, positioning mattered for f_2, f_3, and f_4, but each in their own way. The horizontal symmetry of f_2 might explain why moving the drive and probe in Y does not appear to matter.

For the interaction between the Probe X and Drive X, there is a significant effect on modes f_1 and f_4. For f_4, having Probe and Drive at $X = 0$ had the lowest measured amplitude of any setting; this is odd since there is not a solid node at $X = 0$, but driving anywhere at that

position leads to almost no measured signal averaged over all the $X = 0$ Y positions. Meanwhile, driving and measuring on the left side of the device ($X = -3$) yields the largest amplitude, some 150x that when measured/driven in the middle ($X = 0$). The f_1 mode amplitude is similarly small when measured/driven in the middle ($X = 0$), which does correspond to a node, while it has maximum signal when driven on the left and measured on the right.

Finally, the Drive X and Y positions interact for all modes. Keep in mind, amplitudes are averaged over the entire membrane, so this tells us about drive efficiency. For the f_1 mode, drive efficiency is maximized when driving on the left or right, which corresponds to the antinodes (lobes) of the mode. For f_2, the maximum is driven in the upper-right-hand corner (3,3), corresponding to a lobe. For f_3, maximum occurs in the upper-left-hand corner, which oddly is a sliver of the left antinode. For f_4, the maximum is anywhere on the left side of the membrane, and a minimum on the middle bottom of device, strangely on an antinode.

3.3c Methods for resonator stability experiments

While the actuation efficiency of the drive method differed, we also test the mode frequency stability of each drive method. To do so we tested square-shaped resonators with sizes 7, 10, and 16 μm wide. We tested five resonators twice, once for each drive method. The order of drive method first employed on a given resonator and the order for which resonator would be tested was determined randomly. The only deviation from this randomization was needed to prevent unwanted effects due to heating or photoinduced doping[34]: We ensured that no single resonator was actuated twice in a row without a period of rest while a different resonator was tested. For each test, we continuously swept the drive frequency of the tested method over a range near the fundamental f_0 for a period of at least three hours, yielding multiple spectra of

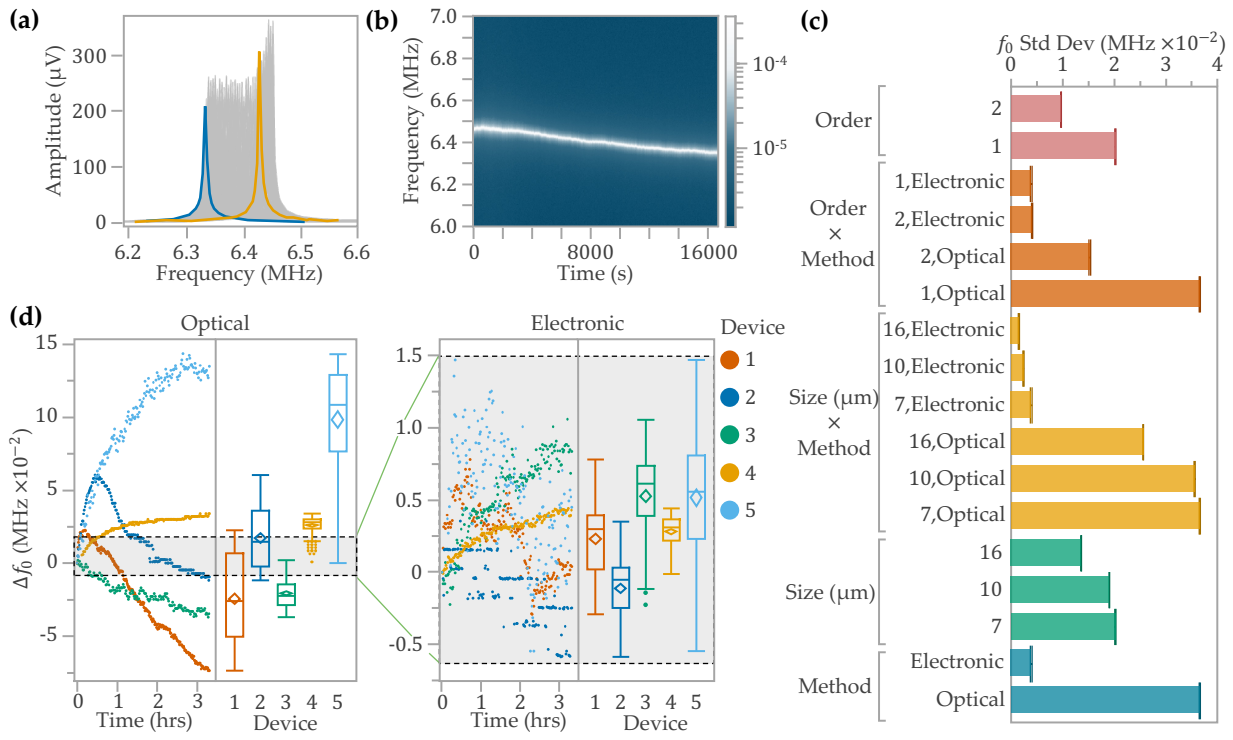


Figure 3.10 Frequency drift

(a) An example of the resonant frequency spectra under continuous frequency sweeping. The gold (right) curve marks the initial sweep while the blue (left) curve marks the last sweep. **(b)** Heatmap of the spectra in (a) over time. The color scale corresponds to the amplitude in (a). **(c)** Factorial mean standard deviations of f_0 by main effects and interactions. The error bars are the standard error. **(d)** The change from the initial fitted fundamental frequency (Δf_0) using outlier box plots and as a function of time. The shaded area corresponds to the same Δf_0 range.

response amplitudes vs frequencies (**Figure 3.10a**). We analyzed the collected spectra to extract the frequency f_{max} and amplitude A_{max} at maximum amplitude and an estimate of the fundamental f_0 of each spectrum, constituting a time-resolved measurement of the drift exhibited via each method (**Figure 3.10b**). To estimate f_0, we fit each spectrum programmatically in MATLAB using

$$R(f) = C + A\frac{f}{\left(f^2 + \left(\frac{Q}{f_0}\right)^2 (f^2 - f_0^2)^2\right)}, \tag{3.1}$$

where R is the LIA's demodulated signal, f is the demodulation frequency, C is a fitting offset, A is the amplitude, Q is the resonator quality factor, and f_0 is the estimated center frequency, following the LIA's fitting model[63].

Our model response variable is the standard deviation of each run's f_0 distribution. We perform a least-squares regression that includes the effects of resonator size, drive method, device run order, the interaction of the run order and drive method, and the interaction of the resonator size and drive method. The results of our modeling are shown in **Figure 3.10c**.

3.3d Stability results

For the drive order, the first run on a device is generally less stable than the second, although the Order × Method interaction highlights that the order difference is dominated by the Optical method as the order does not matter for the electronic method. The increased frequency stability with order in the optical drive method may be due to light field annealing out, ablating off contaminants, or photodoping neutralization; **Figure 3.10d** shows sometimes monotonic behavior.

The f_0 variability goes down as resonator size increases, for both optical and electronic drive, although the optical 10 and 7 μm resonators appear similar. The overall trend of higher stability with increased size may be due to mass adsorption/desorption during the measurement, which would affect the larger resonators less than the smaller ones, since the frequency shift δf (which can be approximated via a Taylor expansion of the frequency $f \approx \sqrt{k/m}$ and using the proportionality of a membrane's mass m to its area a) due to a change in mass δm is

$$\delta f \approx \frac{f}{m}\delta m \propto \frac{1}{a \times a^{\frac{1}{2}}}\ \delta m \propto \frac{1}{a^{\frac{3}{2}}}\ \delta m. \tag{3.2}$$

Thus as m increases with diameter, the frequency shift per change in mass decreases (N.B. k also decreases with diameter). Also, the electronic drive sees a monotonic decrease in the frequency variance, whereas optical drive sees a small change from 7 microns to 10 microns, then a bigger drop for 10 to 16 microns. The drive method affected the variability with the optical exhibiting higher variability by a factor of ~7× that of the electronic.

To further examine the frequency variations differences between optical and electronic drive, we examined the deviation of the frequency from the fundamental mode resonant frequency f_0, denoted Δf_0 for each spectrum (within each test). For each spectrum taken at different time, we measured $\Delta f_0(t) = f_0(t) - f_0$, where f_0 is the fundamental frequency of the first spectrum ($t = 0$). **Figure 3.10d** plots $\Delta f_0(t)$ and the corresponding outlier box plot for five devices and each drive method measured over several hours.

The Δf_0 does not appear to be independently distributed, in general. For the optical drive, Δf_0 has well-defined structure, whereas for the electronic it looks random for some but structured for others. Overall, the optical results do not have a well-defined pattern, with some increasing, peaking, and decreasing, while some increase or decrease monotonically, and some appear to asymptote. However, device 2 exhibits apparent discretization for both optical and electronic driving. Moreover, the noisiest/cleanest resonators tend to be noisy/clean for both measurement techniques. For example, device 5 is the noisiest, while 4 is the cleanest (least noisy).

In optical measurements of NEMS resonators, the spatial relationship between the drive and probe lasers can produce apparent spectral features – such as anti-resonances[64,65] – that stem not from intrinsic resonator dynamics, but from changes in mode shape across the probe location.

We observed multiple apparent single-resonator, anti-resonant spectra (**Figure 3.11a**) during our factorial experiments characterized by a large spectral dip and phase change (**Figure 3.11a**, yellow dashed line) between two resonant modes (green-dashed f_1 and red-dashed f_2).

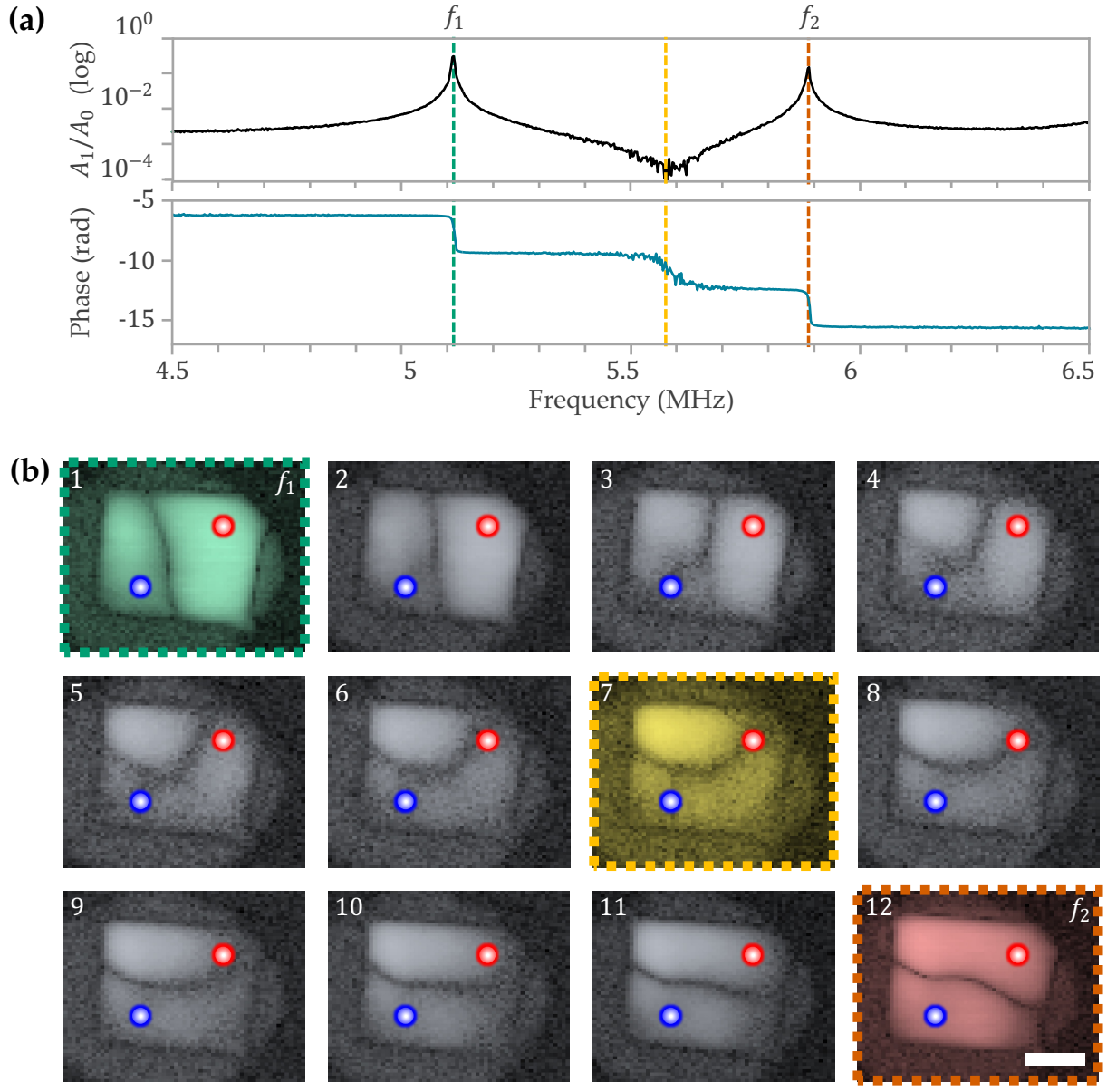


Figure 3.11 Examining apparent anti-resonance

(a) Frequency spectrum with normalized amplitude and phase near f_1 and f_2 for device 2. The phase is unwrapped and corrected for phase drift. **(b)** SIM image sequence for amplitudes between f_1 and f_2 in (a). The locations of the blue drive laser (lower left) and red probe laser (upper right) are superimposed. The dashed border in slide 7 corresponds to the dashed line in (a). The scale bar in frame 12 is 5 μm.

To investigate the apparent anti-resonance, we recorded a sequence of 12 SIM maps taken off resonance, between two adjacent vibrational modes, as shown in **Figure 3.11b**. The drive and probe laser positions are marked as blue and red circles, respectively, corresponding to the configuration used during the spectrum measurement in **Figure 3.11a**. The first frame (outlined in dashed green) was taken at f_1~5.1 MHz, and the last frame (outlined in dashed red) at f_2~5.9 MHz; the seventh frame (outlined in dashed yellow) corresponds to the frequency of the apparent anti-resonance (~5.6 MHz). The sequence reveals a continuous transformation of the nodal pattern from f_1, where the nodal line is roughly vertical, to f_2, where it becomes roughly horizontal. During this evolution in frames 1–5, the upper end of the nodal line remains pinned while the lower portion curves upward, forming a lobe in the upper-left quadrant of the membrane. In frames 6–12, the upper nodal line of the lobe then detaches and migrates toward the right side of the membrane, ultimately forming the horizontal node characteristic of f_2. As the pinned nodal point migrates, the nodal line crosses the probe laser position (frame 7), causing the measured amplitude to drop sharply. These observations indicate that the apparent anti-resonance arises from signal loss as the moving nodal line passes over the probe location. These observations highlight that, in the optical approach, the interplay of drive and probe laser positions can cause nodal line migration to mimic anti-resonance behavior, underscoring the need for spatially resolved mapping to avoid false physical interpretations.

3.4 Discussion

We implemented multiple factorial experiments to elucidate key factors and interactions that affect the frequency stability and access to higher-order modes of a suspended graphene

platform. Generally, electronic driving is substantially more stable than optical driving, even accounting for confounding effects such as resonator size. If frequency stability is important, these results indicate that platforms with electronic driving should be prioritized. While frequency drift exhibited by the resonators showed non-uniform, and often non-monotonic, structure across multiple runs, the drift tended to minimize with time. The shift in f_0 persists across weeks of inactivity, indicating it is not likely a result of photoinduced tuning[34] or temporary heating. Possible candidates for this permanent shift include ablation of contamination material[66,67] and laser-induced damage to the graphene crystal structure[68]. Optical driving more efficiently drives higher-order modes, but the mode shapes need characterization because of the effect of the drive and probe locations. At minimum, optically driving and/or measuring the response at the center of the resonator yields poor amplitude response across higher-order modes compared to other locations. Moreover, laser drift during an experiment can decrease the signal if the probe crosses a node, while the frequency drift can lead to the migration of nodal lines during constant frequency measurements, which can also lead to loss of the signal. Positioning the laser over a node may even lead to that mode being undetected.

4. CONCLUSION

In this work, we performed a systematic, side-by-side comparison of optical and electronic driving methods in suspended graphene NEMS resonators, using factorial experimental designs to isolate and quantify the effects of drive and probe positioning, resonator size, drive method, and drive order on mode accessibility and frequency stability. Our key results show that while optical driving more effectively excites higher-order vibrational modes, it introduces significantly greater frequency instability than electronic driving. We further demonstrate that both the amplitude and stability of driven modes are highly sensitive to the spatial locations of the probe and drive lasers, particularly in optothermal actuation. Time-resolved spectral analysis reveals that frequency drift is not only method-dependent but also device- and time-dependent, exhibiting nonmonotonic evolution and long-term shifts likely caused by permanent physical changes such as laser-induced damage or contaminant ablation. These findings offer a rigorous framework for distinguishing physical effects of actuation in graphene NEMS and establish electronic driving as the preferred method for applications requiring frequency precision and long-term stability. More broadly, this work provides a new quantitative foundation for optimizing NEMS performance and reliability, with implications for sensing, signal processing, and other technologies that rely on mode-selective or stable resonator operation.

REFERENCES CITED

1. Nanoelectromechanical Systems Market Size, Share, Trends [2035]. https://www.globalgrowthinsights.com/market-reports/nanoelectromechanical-systems-market-100699.
2. Dhapte, N. B., Aarti. Nanoelectromechanical Systems Market Size | Share Report 2035. *Market Research Future* https://www.marketresearchfuture.com/reports/nanoelectromechanical-systems-market-8006.
3. Research, M. M. Nanoelectromechanical Systems Market: Size, Dynamics, Regional Insights and Market Segment Analysis. *MAXIMIZE MARKET RESEARCH* https://www.maximizemarketresearch.com/market-report/global-nems-nanoelectromechanical-systems-market/8347/.
4. Nanoelectromechanical Systems Market Share, Size & Forecast. https://www.futuremarketinsights.com/reports/nanoelectromechanical-systems-market.
5. Nanoelectromechanical Systems Market Size, Share & Trends, 2034. *Global Market Insights Inc.* https://www.gminsights.com/industry-analysis/nanoelectromechanical-systems-market.
6. Despont, M. *et al.* VLSI-NEMS chip for parallel AFM data storage. *Sens. Actuators Phys.* **80**, 100–107 (2000).
7. Arcamone, J. *et al.* VLSI silicon multi-gas analyzer coupling gas chromatography and NEMS detectors. in *2011 International Electron Devices Meeting* 29.3.1-29.3.4 (IEEE, Washington, DC, USA, 2011). doi:10.1109/IEDM.2011.6131637.
8. Doster, J. *et al.* Observing polarization patterns in the collective motion of nanomechanical arrays. *Nat. Commun.* **13**, 2478 (2022).
9. Pistolesi, F., Cleland, A. N. & Bachtold, A. Proposal for a Nanomechanical Qubit. *Phys. Rev. X* **11**, 031027 (2021).
10. Matheny, M. H. *et al.* Exotic states in a simple network of nanoelectromechanical oscillators. *Science* **363**, eaav7932 (2019).
11. Craighead, H. G. Nanoelectromechanical Systems. *Science* **290**, 1532–1535 (2000).
12. Li, M., Tang, H. X. & Roukes, M. L. Ultra-sensitive NEMS-based cantilevers for sensing, scanned probe and very high-frequency applications. *Nat. Nanotechnol.* **2**, 114–120 (2007).
13. Luo, G. *et al.* Strong indirect coupling between graphene-based mechanical resonators via a phonon cavity. *Nat. Commun.* **9**, 383 (2018).
14. De Alba, R. *et al.* Tunable phonon-cavity coupling in graphene membranes. *Nat. Nanotechnol.* **11**, 741–746 (2016).
15. Šiškins, M. *et al.* Tunable Strong Coupling of Mechanical Resonance between Spatially Separated $FePS_3$ Nanodrums. *Nano Lett.* **22**, 36–42 (2022).
16. Cha, J. & Daraio, C. Electrical tuning of elastic wave propagation in nanomechanical lattices at MHz frequencies. *Nat. Nanotechnol.* **13**, 1016–1020 (2018).
17. Faust, T., Rieger, J., Seitner, M. J., Kotthaus, J. P. & Weig, E. M. Coherent control of a classical nanomechanical two-level system. *Nat. Phys.* **9**, 485–488 (2013).
18. Huang, P. *et al.* Nonreciprocal Radio Frequency Transduction in a Parametric Mechanical Artificial Lattice. *Phys. Rev. Lett.* **117**, 017701 (2016).

19. Blaikie, A., Miller, D. & Alemán, B. J. A fast and sensitive room-temperature graphene nanomechanical bolometer. *Nat. Commun.* **10**, 4726 (2019).
20. Chaste, J. *et al.* A nanomechanical mass sensor with yoctogram resolution. *Nat. Nanotechnol.* **7**, 301–304 (2012).
21. Lee, C., Wei, X., Kysar, J. W. & Hone, J. Measurement of the Elastic Properties and Intrinsic Strength of Monolayer Graphene. *Science* **321**, 385–388 (2008).
22. Novoselov, K. S. *et al.* Electric Field Effect in Atomically Thin Carbon Films. *Science* **306**, 666–669 (2004).
23. Castro Neto, A. H., Guinea, F., Peres, N. M. R., Novoselov, K. S. & Geim, A. K. The electronic properties of graphene. *Rev. Mod. Phys.* **81**, 109–162 (2009).
24. Changyao Chen & Hone, J. Graphene nanoelectromechanical systems. *Proc. IEEE* **101**, 1766–1779 (2013).
25. Karki, P. & Paulose, J. Stopping and Reversing Sound via Dynamic Dispersion Tuning in a Phononic Metamaterial. *Phys. Rev. Appl.* **15**, 034083 (2021).
26. Jadhav, S. *et al.* HZO-based FerroNEMS MAC for in-memory computing. *Appl. Phys. Lett.* **121**, 193503 (2022).
27. Bonnin, M., Traversa, F. L. & Bonani, F. Coupled oscillator networks for von Neumann and non von Neumann computing. Preprint at http://arxiv.org/abs/2012.12386 (2020).
28. Mouharrar, H. *et al.* Generation of Soliton Frequency Combs in NEMS. *Nano Lett.* https://doi.org/10.1021/acs.nanolett.4c02249 (2024) doi:10.1021/acs.nanolett.4c02249.
29. Keşkekler, A., Bos, V., Aragón, A. M., Steeneken, P. G. & Alijani, F. Multimode Nonlinear Dynamics of Graphene Resonators. *Phys. Rev. Appl.* **20**, 064020 (2023).
30. Xu, J., Wood, Graham. S., Mastropaolo, E., Newton, Michael. J. & Cheung, R. Realization of a Graphene/PMMA Acoustic Capacitive Sensor Released by Silicon Dioxide Sacrificial Layer. *ACS Appl. Mater. Interfaces* **13**, 38792–38798 (2021).
31. Šiškins, M. *et al.* Sensitive capacitive pressure sensors based on graphene membrane arrays. *Microsyst. Nanoeng.* **6**, 102 (2020).
32. Chen, M. E. *et al.* Graphene-based electromechanical thermal switches. *2D Mater.* **8**, 035055 (2021).
33. Sun, J., Schmidt, M. E., Muruganathan, M., Chong, H. M. H. & Mizuta, H. Large-scale nanoelectromechanical switches based on directly deposited nanocrystalline graphene on insulating substrates. *Nanoscale* **8**, 6659–6665 (2016).
34. Miller, D., Blaikie, A. & Alemán, B. J. Nonvolatile Rewritable Frequency Tuning of a Nanoelectromechanical Resonator Using Photoinduced Doping. *Nano Lett.* **20**, 2378–2386 (2020).
35. Mei, T., Lee, J., Xu, Y. & Feng, P. Frequency Tuning of Graphene Nanoelectromechanical Resonators via Electrostatic Gating. *Micromachines* **9**, 312 (2018).
36. Okamoto, H. *et al.* A strongly coupled Λ-type micromechanical system. *Appl. Phys. Lett.* **108**, 153105 (2016).
37. Lin, S. *et al.* Realization of programmable nanomechanical lattice with both nearest-neighboring and next-nearest-neighboring couplings. *Appl. Phys. Lett.* **117**, 093503 (2020).
38. Doster, J., Hoenl, S., Lorenz, H., Paulitschke, P. & Weig, E. M. Collective dynamics of strain-coupled nanomechanical pillar resonators. *Nat. Commun.* **10**, 5246 (2019).
39. Keşkekler, A. *et al.* Tuning nonlinear damping in graphene nanoresonators by parametric–direct internal resonance. *Nat. Commun.* **12**, 1099 (2021).

40. Li, D., Yan, J., Zhang, Y., Wang, J. & Yu, L. Lorentz Force-Actuated Bidirectional Nanoelectromechanical Switch with an Ultralow Operation Voltage. *Nano Lett.* https://doi.org/10.1021/acs.nanolett.4c01999 (2024) doi:10.1021/acs.nanolett.4c01999.
41. Lin, S. *et al.* Realization of programmable nanomechanical lattice with both nearest-neighboring and next-nearest-neighboring couplings. *Appl. Phys. Lett.* **117**, 093503 (2020).
42. Yang, R. *et al.* Raman Spectroscopic Probe for Nonlinear MoS_2 Nanoelectromechanical Resonators. *Nano Lett.* **22**, 5780–5787 (2022).
43. Pelka, K., Madiot, G., Braive, R. & Xuereb, A. Floquet Control of Optomechanical Bistability in Multimode Systems. *Phys. Rev. Lett.* **129**, 123603 (2022).
44. Xie, Y.-J., Zhang, M.-N., Wang, R., Wang, L.-F. & Huang, Q.-A. Experimental realization of tunable Fano resonances in two coupled silicon micromechanical resonators. *Phys. Rev. Res.* **7**, 013002 (2025).
45. Zhang, P., Jia, Y., Yuan, S., Liu, Z. & Yang, R. Tunable Stochastic State Switching in 2D MoS2 Nanomechanical Resonators with Nonlinear Mode Coupling and Internal Resonance. *Nano Lett.* https://doi.org/10.1021/acs.nanolett.4c03173 (2024) doi:10.1021/acs.nanolett.4c03173.
46. Fan, X. *et al.* Graphene MEMS and NEMS. *Microsyst. Nanoeng.* **10**, 154 (2024).
47. Miller, D. & Alemán, B. Spatially resolved optical excitation of mechanical modes in graphene NEMS. *Appl. Phys. Lett.* **115**, 193102 (2019).
48. Davidovikj, D. *et al.* Visualizing the Motion of Graphene Nanodrums. *Nano Lett.* **16**, 2768–2773 (2016).
49. Novotny, L. Strong coupling, energy splitting, and level crossings: A classical perspective. *Am. J. Phys.* **78**, 1199–1202 (2010).
50. Vibrating Membrane. *COMSOL* https://www.comsol.com/model/vibrating-membrane-12587.
51. Barton, R. A. *et al.* Photothermal Self-Oscillation and Laser Cooling of Graphene Optomechanical Systems. *Nano Lett.* **12**, 4681–4686 (2012).
52. Bunch, J. S. *et al.* Electromechanical Resonators from Graphene Sheets. *Science* **315**, 490–493 (2007).
53. Metzger, C., Favero, I., Ortlieb, A. & Karrai, K. Optical self cooling of a deformable Fabry-Perot cavity in the classical limit. *Phys. Rev. B* **78**, 035309 (2008).
54. Montgomery, D. C. *Design and Analysis of Experiments*. (John Wiley & Sons, Inc., 2013).
55. UniversityWafer, Inc. Silicon Wafers, other substrates for research and industry. https://www.universitywafer.com/index.html.
56. Graphenea. Graphene on Your Substrate. https://www.graphenea.com/products/graphene-on-your-substrate.
57. Carter, B. E. Building and Characterizing Graphene Nanomechanical Resonator Networks. *ProQuest Dissertations and Theses* (University of Oregon, United States -- Oregon, 2023).
58. Yang, R., Zheng, X., Wang, Z., Miller, C. J. & Feng, P. X.-L. Multilayer MoS2 transistors enabled by a facile dry-transfer technique and thermal annealing. *J. Vac. Sci. Technol. B Nanotechnol. Microelectron. Mater. Process. Meas. Phenom.* **32**, 061203 (2014).
59. Riyahi, M., Parsanasab, G.-M. & Sabaeian, M. Graphene patterning without plasma etching via SU-8 pattern peel-off. *Sci. Rep.* **15**, 23910 (2025).

60. Double Sided Polyimide Tapes, UL Recognized, 36 Yards Long. *KaptonTape* https://kaptontape.com/product/double-sided-polyimide-tapes-rohs-compliant-36-yards-long-2/.
61. MATLAB. https://www.mathworks.com/products/matlab.html.
62. Predictive Analytics Software. https://www.jmp.com/en/software/predictive-analytics-software.
63. Zurich Instruments AG. HF2 User Manual (Revision 25.04). (2025).
64. Wang, G. *et al.* A Review on Resonant MEMS Electric Field Sensors. *Micromachines* **15**, 1333 (2024).
65. Liu, J.-R. *et al.* Vibration Mode Suppression in Micromechanical Resonators Using Embedded Anti- Resonating Structures. *J. Microelectromechanical Syst.* **30**, 53–63 (2021).
66. Mackenzie, D. M. A. *et al.* Fabrication of CVD graphene-based devices via laser ablation for wafer-scale characterization. *2D Mater.* **2**, 045003 (2015).
67. Panyathip, R., Choopun, S., Singjai, P. & Sakulsermsuk, S. Utilizing laser scribing for graphene ablation. *AIP Adv.* **11**, 105305 (2021).
68. Currie, M. *et al.* Quantifying pulsed laser induced damage to graphene. *Appl. Phys. Lett.* **99**, 211909 (2011).